A Volcano Rekindled: The Renewed Eruption of Mount St. Helens, 2004–2006
Edited by David R. Sherrod, William E. Scott, and Peter H. Stauffer
U.S. Geological Survey Professional Paper 1750, 2008

Chapter 21

Dynamics of Seismogenic Volcanic Extrusion Resisted by a Solid Surface Plug, Mount St. Helens, 2004–2005

By Richard M. Iverson[1]

Abstract

The 2004–5 eruption of Mount St. Helens exhibited sustained, near-equilibrium behavior characterized by nearly steady extrusion of a solid dacite plug and nearly periodic occurrence of shallow earthquakes. Diverse data support the hypothesis that these earthquakes resulted from stick-slip motion along the margins of the plug as it was forced incrementally upward by ascending, solidifying, gas-poor magma. I formalize this hypothesis with a mathematical model derived by assuming that magma enters the base of the eruption conduit at a steady rate, invoking conservation of mass and momentum of the magma and plug, and postulating simple constitutive equations that describe magma and conduit compressibilities and friction along the plug margins. Reduction of the model equations reveals a strong mathematical analogy between the dynamics of the magma-plug system and those of a variably damped oscillator. Oscillations in extrusion velocity result from the interaction of plug inertia, a variable upward force due to magma pressure, and a downward force due to the plug weight. Damping of oscillations depends mostly on plug-boundary friction, and oscillations grow unstably if friction exhibits rate weakening similar to that observed in experiments. When growth of oscillations causes the extrusion rate to reach zero, however, gravity causes friction to reverse direction, and this reversal instigates a transition from unstable oscillations to self-regulating stick-slip cycles. The transition occurs irrespective of the details of rate-weakening behavior, and repetitive stick-slip cycles are, therefore, robust features of the system's dynamics. The presence of a highly compressible elastic driving element (that is, magma containing bubbles) appears crucial for enabling seismogenic slip events to occur repeatedly at the shallow earthquake focal depths (<1 km) observed during the 2004–5 eruption. Computations show that fluctuations in magma pressure accompanying such slip events are <3 kPa, indicating that deviations from mechanical equilibrium are slight and that coseismic force drops are $<10^8$ N. These results imply that the system's self-regulating behavior is not susceptible to dramatic change—provided that the rate of magma ascent remains similar to the rate of magma accretion at the base of the plug, that plug surface erosion more or less compensates for mass gain due to basal accretion, and that magma and rock properties do not change significantly. Even if disequilibrium initial conditions are imposed, the dynamics of the magma-plug system are strongly attracted to self-regulating stick-slip cycles, although this self-regulating behavior can be bypassed on the way to runaway behavior if the initial state is too far from equilibrium.

Introduction

The dome-building eruption of Mount St. Helens that began in October 2004 was remarkable in several respects. This paper describes formulation, analysis, and predictions of a mechanistic model that links three key aspects of the eruption. The first and perhaps most striking of these aspects was extrusion of solid rock that emerged from the crater floor as a sequence of spines with conspicuous fault gouge and striations on their freshly exposed bounding surfaces. Second, extrusion proceeded at a nearly constant long-term rate (~1–2 m^3/s) that was sustained from December 2004 through at least December 2005. Third, extrusion was accompanied by more than a million small earthquakes that occurred almost periodically at hypocentral locations <1 km beneath the extruding dome. These eruption characteristics motivate the hypothesis that extrusion was driven by a nearly constant influx of magma at depth and resisted by a plug of solidified magma that slipped incrementally and seismogenically against the wall rock forming the upper parts of the magma conduit. I refer to this hypothesis as SPASM, an acronym for Seismogenic Plug of Ascending, Solidifying Magma.

[1] U.S. Geological Survey, 1300 SE Cardinal Court, Vancouver, WA 98683

This paper formalizes the SPASM hypothesis mathematically and tests whether it is consistent quantitatively with behavior observed during the 2004–5 eruption of Mount St. Helens. The mechanistic framework of the SPASM model is simple, reflecting my belief that a relatively simple physical process (that is, one involving few special conditions and contingencies) is most likely responsible for producing persistent, repetitive, natural events—such as nearly periodic earthquakes. Although the SPASM model aims chiefly to explain the origin of these earthquakes, it can also provide insight into conditions under which the eruption style might significantly change, and the potential for such change has large implications for assessment of volcano hazards.

Below, following a brief overview of key features of the 2004–5 eruption of Mount St. Helens, I describe the conceptual basis of the SPASM model. I then present the mathematical formulation of the nonlinear SPASM equations and analytical results obtained from exact solutions of approximate (that is, linearized) versions of these equations. The analytical results demonstrate the plausibility of several broad classes of eruptive behavior, including both stable and unstable behavior. I then use numerical results obtained from approximate solutions of the exact, nonlinear model equations to clarify some consequences of instability. In particular, the numerical results show how stick-slip motion arises as a natural consequence of plug extrusion dynamics. In the final sections of the paper, I discuss implications of these findings for interpreting solid-state volcanic extrusion and accompanying seismicity.

Eruption Overview

Despite Mount St. Helens' famous explosive eruption in 1980, the dome-building activity that began in 2004 is consistent with the volcano's recent geologic history (Mullineaux and Crandell, 1981). Over the past ~4,000 years, Mount St. Helens has extruded rock at a mean rate of about 0.2 m^3/s while constructing a 26-km^3 modern edifice (defined here as the volume above 1,220 m altitude) composed primarily of andesite and dacite lava flows and domes and their detritus. From 1980 to 1986 a dacite dome grew episodically in the crater formed during the 1980 eruption, and its volume ultimately reached 7.4×10^7 m^3 (Swanson and Holcomb, 1990). From 1987 to 2004 Mount St. Helens did not erupt, although at least six phreatic explosions occurred from 1989 to 1991 (Mastin, 1994). Recurrent seismicity at depths of 2–8 km in the late 1980s and 1990s may have been associated with magma recharge but did not lead to eruptions (Moran, 1994).

Renewed eruptive activity began on October 1, 2004, when a small explosion formed a vent through the ~150-m-thick glacier that had grown in the southern part of Mount St. Helens' crater since 1986 (Schilling and others, 2004; Dzurisin and others, 2005; Walder and others, 2005). The explosion was preceded by about 7 days of increasingly intense seismicity at depths <1 km, but deeper seismicity (such as might be indicative of magma-chamber pressurization or depressurization) did not occur then and has not occurred subsequently (Moran and others, this volume, chap. 2). By October 11, explosions had largely ceased, seismic energy release had decreased to a rate about one-tenth that of the preceding two weeks, and extrusion of a solid dacite plug had begun (Dzurisin and others, 2005). By December 2004, extrusion rates had become nearly steady, and by December 15, 2005, the volume of the resulting new lava dome was ~7.3×10^7 m^3 (Schilling and others, this volume, chap. 8). This volume, added to that of the 1980–86 lava dome, implies that the mean extrusion rate at Mount St. Helens from 1980 to 2005 was about 0.2 m^3/s, similar to the mean rate for the past 4,000 years. Thus, the 2004–5 activity of Mount St. Helens was by no means unusual.

The remainder of this section focuses on the quasi-steady eruptive behavior observed at Mount St. Helens from December 2004 through December 2005, because understanding this behavior is the goal of SPASM. Other papers in this volume provide detailed descriptions of the findings briefly summarized below.

Extrusion Rates and Vent Size

After extrusion commenced, it appeared to occur continuously through December 2005, and it produced a sequence of monolithic dacite spines, with some reaching heights >100 m. The fourth of these spines had such a strikingly smooth, symmetrical, elongate form that it resembled a breaching whale and was accordingly dubbed the "whaleback" (fig. 1). Each spine emerged over a period of several weeks to several months and eventually disintegrated as a consequence of fracturing and avalanching of rock from its exposed surfaces. By late 2005, the sequence of spines had formed a composite dome with the appearance of a multicrested pile of rubble, and distinguishing individual spines would in retrospect have been difficult without knowledge of their emplacement history.

Despite the rather complicated details of spine emplacement, photogrammetric analysis showed that the rate of extrusion remained remarkably constant from about December 2004 to December 2005 (fig. 2) and typically ranged from about 1 to 2 m^3/s (Schilling and others, this volume, chap. 8). During the same period, the linear extrusion rate (that is, the speed of spine emergence from the ground) estimated from far-field, ground-based photography typically ranged from about 3×10^{-5} to 7×10^{-5} m/s (3–6 m/day) (Major and others, this volume, chap. 12), and these rates were largely consistent with high-precision data transmitted by short-lived GPS receivers placed intermittently on the extruding spines (LaHusen and others, this volume, chap. 16). Similar linear extrusion rates were inferred from short-duration, short-range photography, which detected centimeter-scale plug emergence over durations as brief as a few minutes (Dzurisin and others, this volume, chap. 14). Thus, all evidence indicates that extrusion rates were essentially constant over time scales longer than the duration of small earthquakes (about 10 s or less) but shorter than the multiyear duration of the eruption as a whole (>10^7 s).

According to the SPASM hypothesis, small, abrupt pulses in plug extrusion were responsible for generating small earthquakes. These pulses would have typically entailed upward plug displacements of ~5 mm (a value obtained by multiplying the typical 5×10^{-5} m/s linear extrusion rate by the typical 100-s interval between earthquakes), but abrupt movements this small were not resolvable by displacement measurements. Moreover, abrupt slip occurring at earthquake hypocentral depths may have been muted at shallower depths owing to inelastic deformation of weak near-surface materials. As a consequence, no direct measurements of coseismic pulses of plug extrusion were made during the eruption. Therefore, the SPASM model addresses the dynamics of stick-slip cycles with properties that have been inferred but not directly measured.

Inference also plays a role in estimating the size of the vent where extruding spines breached the crater floor, because the presence of fragmented glacier ice and accumulated talus, as well as previously extruded rock, partly obscured the vent margins. Moreover, different parts of the vent became visible as successive spines emerged and moved laterally as well as upward. From the standpoint of constraining the SPASM model, the most useful estimates of the effective cross-sectional area of the vent are obtained not from direct observations of spine geometry but from comparison of volumetric and linear extrusion rates measured over extended periods. Division of the typical volumetric rate of 1.5 m^3/s by the typical linear rate of 5×10^{-5} m/s yields an effective vent area of 30,000 m^2, which implies an effective vent diameter of ~200 m if the vent geometry is assumed to be circular. A vent of this size (but not necessarily circular) is assumed for all calculations I present in this paper.

Gouge Properties

Where fresh surfaces of newly extruded spines were exposed, they were coated with granulated, striated dacite interpreted to be fault gouge. The gouge presumably formed as a consequence of mechanical wear during localized shearing along the margins of the dacite plug as it moved upward relative to the adjacent conduit walls (compare Tuffen and Dingwell, 2005). Observations and dredge sampling from hovering helicopters indicated that the gouge thickness was typically about 1 m (J.S. Pallister, U.S. Geological Survey, oral commun., 2005). Striations on the gouge surface were abundant and generally aligned with the direction of extrusion (fig. 3).

Frictional properties of the gouge were measured using a large-scale ring-shear apparatus, in which a remolded, annular specimen (~0.012 m^3) was deformed in simple shear at various imposed rates (Moore and others, this volume, chap. 20). The measurements demonstrated that the gouge typically exhibited peak strength at displacements <0.5 mm, steady-state strength after about 3 mm of displacement, and reduction of steady-state strength with increasing shear rate (for example, fig. 4). At rates $\geq5\times10^{-4}$ m/s (about 43 m/day), this rate-weakening

Figure 1. Oblique aerial photograph of extruding "whaleback" spine 4 at Mount St. Helens, viewed from the northwest, on February 22, 2005. Horizontal length of the smooth whaleback is about 380 m. Arrow shows vent from which the spine emerged. USGS photo by S.P. Schilling.

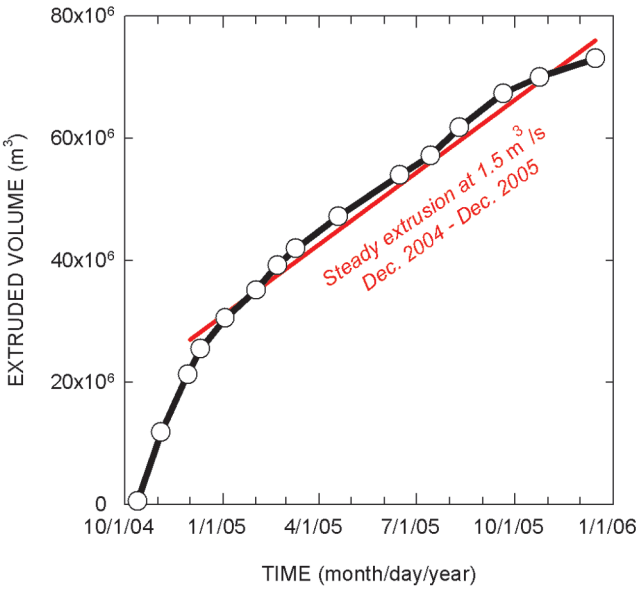

Figure 2. Measured volume of extruded dome rock at Mount St. Helens as a function of time (after Schilling and others, this volume, chap. 8). The red reference line shows growth of dome volume occurring with a constant extrusion rate of 1.5 m^3/s from December 2004 to December 2005.

behavior was supplanted by rate-strengthening behavior, but the relevance of this transition is questionable because the test equipment could shear the specimen at rates $\geq 5\times10^{-4}$ m/s only under very low confining stresses, ≤23 kPa (Moore and others, this volume, chap. 20).

Overall, the ring-shear tests of Moore and others (this volume, chap. 20) showed that frictional behavior of the Mount St. Helens gouge was largely consistent with that expected from models of rate- and state-dependent friction (for example, Dieterich, 1979; Ruina, 1983; Marone, 1998). Such models posit that frictional strength varies in proportion to the logarithms of the imposed shear rate and hold time (that is, the time a specimen is held in a static state between successive shear events). In rate-weakening materials, the combined effect of shear rate and hold time causes a reduction of frictional strength as steady shear rates increase. In tests of the Mount St. Helens fault gouge under confining stresses of 86–195 kPa, measured values of steady-state friction coefficients ranged from 0.42 to 0.47, and these values declined logarithmically as the imposed shear rate increased (Moore and others, this volume, chap. 20). Measured peak friction coefficients were 1–9 percent larger than steady-state friction coefficients, and peak values increased logarithmically with hold time. This hold-time effect is typical of rocks and densely packed granular materials (for example, Beeler and others, 1994; Losert and others, 2000).

Testing by Moore and others (this volume, chap. 20) also revealed that the effective in-place shear stiffness of the gouge was probably orders of magnitude larger than the effective stiffness of the magma body that loaded the gouge as it pushed the extruding plug upward. This contrast in stiffness, along with rate-weakening steady-state friction, provides a sufficient condition for stick-slip behavior in materials exhibiting rate- and state-dependent friction (Rice and Ruina, 1983; Ruina, 1983).

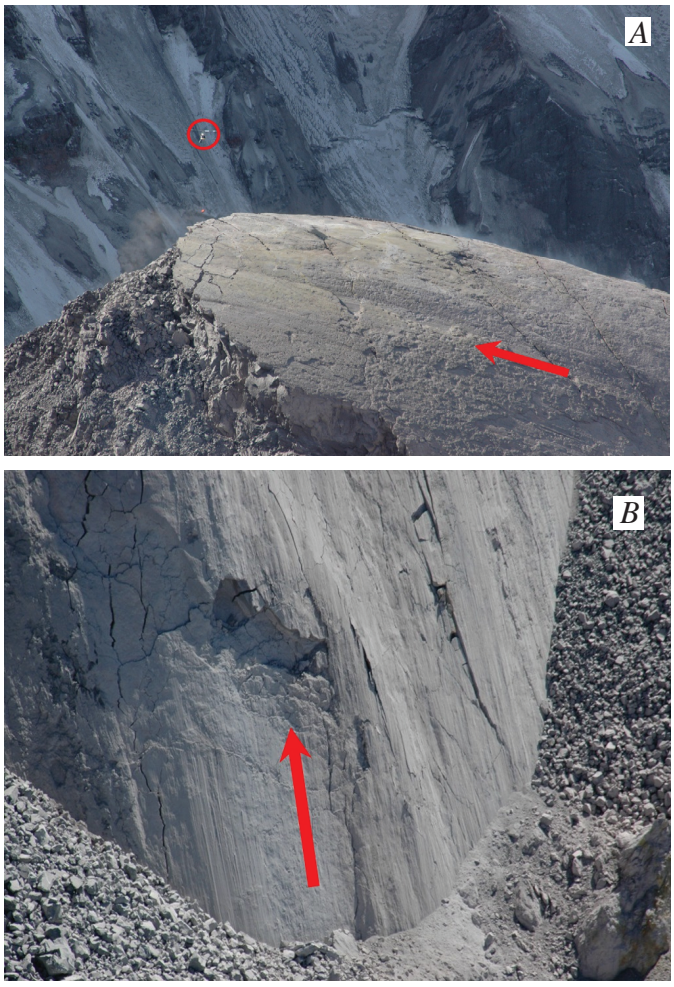

Figure 3. Photographs of striated, gouge-coated surfaces of extruding spines at Mount St. Helens. Arrows show direction of spine motion. *A*, Crest of spine 4 viewed from east on February 22, 2005. Hovering helicopter (circled) provides scale. *B*, Base of spine 5 viewed from north on July 28, 2005. Field of view is roughly 30 m wide. USGS photos by S.P. Schilling.

Drumbeat Earthquakes

An extraordinary feature of the 2004–5 eruption of Mount St. Helens was persistence of small ($M_d \leq 2$), shallow earthquakes that recurred so regularly they were dubbed "drumbeats" (Moran and others, this volume, chap. 2). The period between successive drumbeats shifted slowly with time but was commonly ~100 s (for example, fig. 5) and nearly always in the range 30–300 s. Seismograms showed that

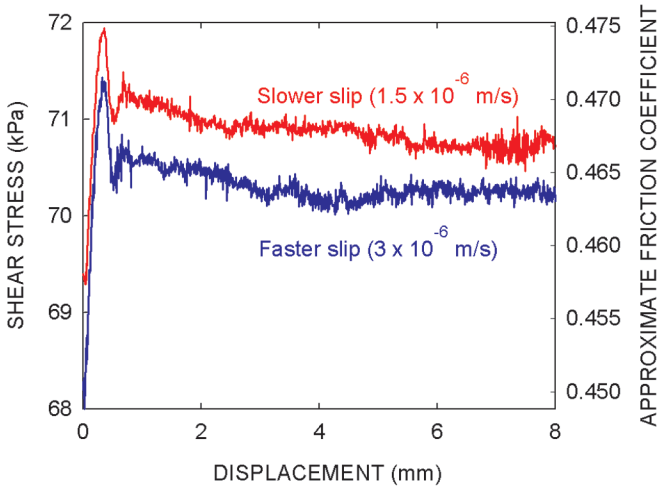

Figure 4. Example of data collected during ring-shear tests of gouge friction by Moore and others (this volume, chap. 20). Measured shear stress as a function of displacement is shown for two steady-state shear rates. Inferred friction coefficients (right-hand axis) represent shear stress divided by a nominally constant normal stress of 159 kPa, but normal stress fluctuated slightly (<1 percent) during the tests, such that friction coefficients are approximate (after Moore and others, this volume, chap. 20).

drumbeat waveforms generally had impulsive, high-frequency onsets and low-frequency codas, similar to waveforms of other hybrid volcanic earthquakes (for example, Lahr and others, 1994; Neuberg, 2000). Over time scales of hours to weeks, drumbeats typically had consistent sizes and did not display a Gutenberg-Richter magnitude-frequency distribution typical of tectonic earthquakes (Moran and others, this volume, chap. 2). Precise location of drumbeat hypocenters was hindered by the geologic and topographic complexity of the Mount St. Helens crater and the low density of crater seismometers, but within resolution limits (~100 m), all drumbeats originated at depths <1 km directly around or beneath the growing dome. Accompanying the drumbeats at irregular intervals were smaller and larger earthquakes (as large as M_d 3.4) with differing seismic signatures, but these earthquakes had little lasting effect on the drumbeats.

The recurrence and character of drumbeat earthquakes implies the existence of a nondestructive seismic source, as has been inferred for other repetitive volcanic earthquakes (Lahr and others, 1994; Goto, 1999; Neuberg, 2000; Neuberg and others, 2006). The most outstanding attribute of the drumbeat earthquakes at Mount St. Helens, however, was their periodicity. This periodicity, together with the presence of striated fault gouge bounding the extruding plug, is the key motivation for the SPASM hypothesis.

Although the SPASM model aims to link plug extrusion and earthquake generation, it does not address resulting seismic radiation. Radiation of seismic waves could result from rapid propagation of rupture that spreads along the fault surface after nucleating in a strong "keystone" patch of fault gouge (see Scholz, 2002). Alternatively, the force drop accompanying frictional slip that occurs uniformly along the plug margins might be so abrupt as to radiate seismic energy (see Marone and Richardson, 2006), and this force drop is calculated by the SPASM model. In relating SPASM mechanics to seismic radiation, however, it must be borne

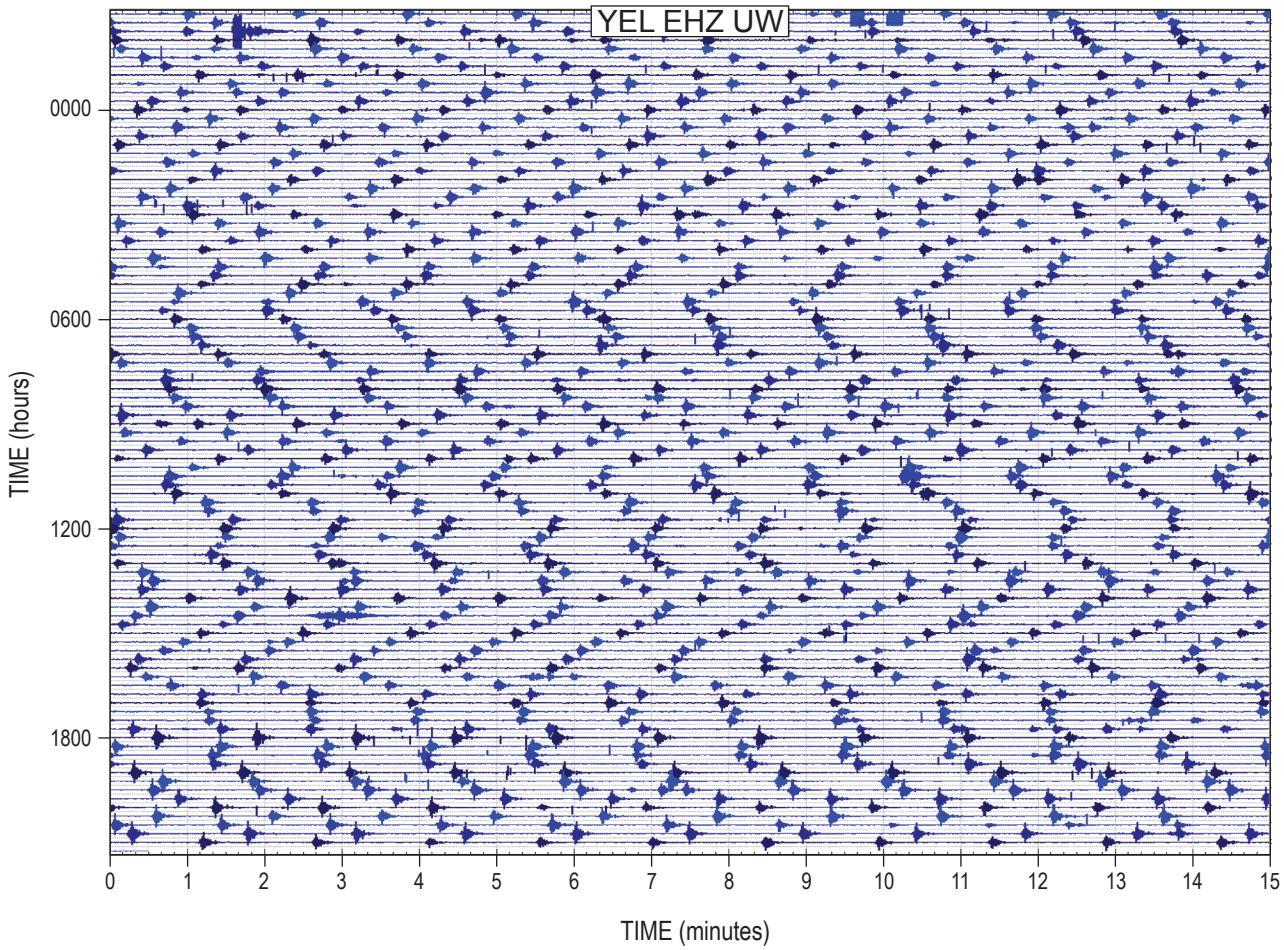

Figure 5. Example of 24-hour seismogram illustrating nearly periodic occurrence of "drumbeat" earthquakes at Mount St. Helens. Graph shows seismicity recorded at station YEL, located 1.5 km north of the 2004–5 vent. Time begins at 21:00 UTC on December 1, 2005, and scrolls from left to right and then top to bottom. Earthquake magnitudes were roughly 0.5–1 during this interval. Data courtesy of Pacific Northwest Seismic Network.

in mind that only a small fraction (<10 percent) of the work done during fault slip typically results in seismic radiation (McGarr, 1999). Generally, more work is done in overcoming friction, and the mechanics of the total work cycle is the primary focus of SPASM.

Magma Solidification and Compressibility

Although genesis of the magma that erupted in 2004–5 remains uncertain, petrologic data indicate that solidification occurred at depths <1 km. This inference derives from the fact that the composition of glass in the newly erupted dacite plots between the 0.1 and 50 MPa cotectics of the modified quartz-albite-orthoclase phase diagram for Mount St. Helens dacites (Blundy and Cashman, 2001) and from the presence of tridymite, which constrains the late stages of solidification to pressures of 10–20 MPa (equivalent to estimated lithostatic pressures at depths ~0.5–1 km) (Pallister and others, 2005, and this volume, chap. 30). These depths are consistent with the maximum hypocentral depths inferred for drumbeat earthquakes (Moran and others, this volume, chap. 2), and they imply that solid-state extrusion and earthquake generation were collocated.

The quantity and composition of volcanic gases emitted during the 2004–5 eruption demonstrate that the magma was gas poor in comparison to the 1980 Mount St. Helens magma but that the 2004–5 magma nonetheless contained sufficient exsolved gas to greatly influence its compressibility. At 8 km depth the gas volume fraction was probably <2 percent, but calculations using methods of Newman and Lowenstern (2002) indicate that the gas volume fraction grew during magma ascent and reached about 50 percent at ~1 km depth, where solidification began (Gerlach and others, this volume, chap. 26). The same calculations indicate that at depths between 8 and 1 km, the gas volume fraction averaged ~12 percent. Allowing for inevitable gas separation from rock during extrusion, these results are consistent with observed vesicle volume fractions of 11–34 percent in samples of the 2004–5 dacite (Gerlach and others, this volume, chap. 26). An exsolved gas volume fraction of 12 percent implies a magma compressibility ~10^{-7} Pa^{-1}, according to the model of Mastin and Ghiorso (2000). Although this value is, of course, inexact, its mechanical significance is clear: the magma was almost certainly much more compressible than solid rock, which generally has compressibilities <10^{-10} Pa^{-1} (Hatheway and Kiersch, 1989). As a consequence, magma compression almost certainly dominated elastic strain as pressure within the magma-conduit-plug system increased.

Geodetic Inferences About Magma Influx

Measured displacements of the volcano flanks and adjacent areas preceding and during the 2004–5 eruption imply that the volume of magma evacuated from depths <10 km was considerably less than the volume of extruded rock (Lisowski and others, this volume, chap. 15). No evidence of systematic preeruption surface displacement was found by global positioning system (GPS) surveys in 2000 and 2003 of a 40-station network centered on the volcano, nor by continuous operation of GPS station JRO1, located 9 km north of the eruption vent. Seismicity that heralded the eruption in late September 2004 was accompanied by only centimeter-scale downward and southward (that is, inward) surface displacements at JRO1 (Lisowski and others, this volume, chap. 15). The displacement pattern measured at all stations corresponds well with that predicted by an elastic half-space model that assumes pressure decrease within a vertically oriented, prolate spheroidal cavity with a mean depth of 8 km and volume loss ~2×10^7 m^3 during the period from October 1, 2004, to November 25, 2005 (Lisowski and others, this volume, chap. 15). This apparent volume loss is less than one-third the volume of rock extruded during the same period, and little of the apparent volume loss occurred after the onset of nearly steady extrusion in December 2004, implying that magma recharge from a deep (>10 km) source accompanied this phase of the eruption.

Conceptual Basis of Mathematical Model

The basic mechanical elements of the SPASM model are shown schematically in figure 6, and table 1 defines all mathematical symbols used in development and analysis of the model. The model assumes that magma flows into the base of a feeder conduit at a steady volumetric rate Q. The conduit is assumed to originate about 8 km beneath the Mount St. Helens crater, a depth inferred from hypocentral locations of pre-2004 earthquakes apparently associated with magma movement (Moran, 1994; Moran and others, this volume, chap. 2). Ascent of magma at the top of the conduit is resisted by force exerted by a near-surface plug of solidified magma, owing to its weight mg and boundary friction F. Seismic and petrologic data collected during the 2004–5 eruption imply that the plug extends to a depth <1 km, and as a baseline value I assume that it extends to a depth ~500 m. The plug mass m can change with time as a consequence of basal accretion of congealing magma at mass rate ρB, where ρ is the magma bulk density, and as a consequence of surface erosion by spalling and avalanching at mass rate $\rho_r E$, where ρ_r is the bulk density of the plug rock. The conduit volume can change with time as a result of motion of the base of the plug and changes in magma pressure that cause elastic deflection of the conduit walls. The magma pressure and density can change in response to the changing balance between the steady magma influx and changing conduit volume. The resulting mathematical model represents the simultaneous evolution of the upward plug velocity u, magma pressure against the base of the plug p, and conduit volume V, which are influenced by concurrent evolution of m and ρ.

Implicit in the SPASM model is a "top-down" perspective of eruption dynamics. The model focuses on observed surface and near-surface phenomena associated with eruptive behavior but does not consider phenomena associated with unobserved changes that might occur in a deep magma reservoir. Instead, in the SPASM model, variations in extrusion rate are postulated to arise naturally as a consequence of the dynamics of the solid plug responding to steady forcing. Unsteady forcing due to unsteady magma influx would complicate behavior exhibited by the SPASM model but would not change its fundamental character.

The SPASM model is one-dimensional and does not explicitly consider the effects of conduit and plug geometry. This simplification poses both an advantage and disadvantage. The advantage derives from the fact that predictions of the SPASM model are independent of geometrical effects and are, in a general sense, applicable to any geometry. The disadvantage is that SPASM yields no insight concerning the effects of geometrical complications such as variations in the shape of the magma conduit, vent, or growing lava dome.

Many previous eruption models have used a one-dimensional approach similar to the one used here, and some models have invoked stick-slip motion as a phenomenon responsible for cyclical eruptive behavior (for example, Denlinger and Hoblitt, 1999; Voight and others, 1999; Ozerov and others, 2003). The SPASM model, however, is the first to demonstrate how stick-slip behavior arises as a natural consequence of system dynamics. Indeed, a key feature of the SPASM model is that forces need not be balanced; therefore, the model can exhibit dynamical behavior not possible in eruption models that assume balanced forces (for example, Mastin and others, this volume, chap. 22).

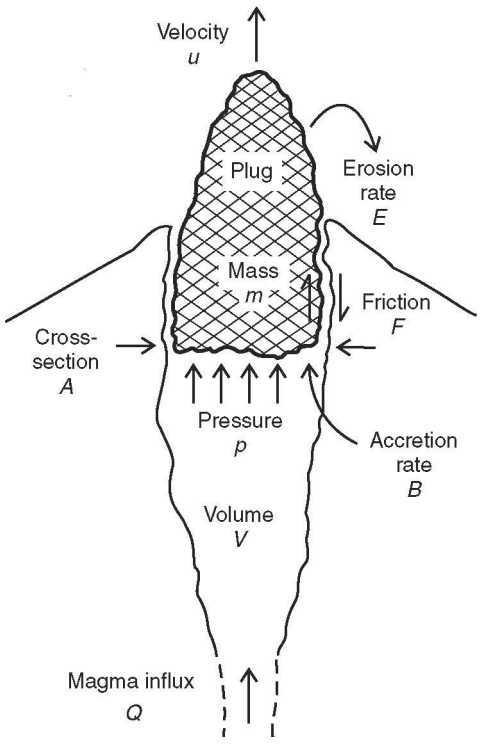

Figure 6. Schematic diagram illustrating the conceptual framework of the SPASM model.

Mathematical Formulation

The most fundamental equations used to derive the SPASM model express conservation of mass and linear momentum of the solid plug and conduit fluid. These conservation laws are supplemented by constitutive equations defining magma compressibility, conduit wall-rock compliance, and the frictional force acting where the plug contacts the conduit walls. In this section the conservation and constitutive equations are presented and reduced to a set of three simultaneous differential equations that describe behavior of the magma-conduit-plug system as a whole.

Conservation of Linear Momentum of Solid Plug

Changes in the upward momentum of the solid plug are described by Newton's second law of motion, expressed as

$$m\frac{du}{dt}+u\frac{dm}{dt} = p\,A - m\,g - F, \qquad (1)$$

where m is the plug mass, u is the vertical (upward) plug velocity, g is the magnitude of gravitational acceleration, and p is the magma pressure against the base of the plug, which has area A in horizontal projection. Upward motion of the plug is driven by the basal magma-pressure force pA and resisted by the plug weight mg and boundary friction force F. Implicit in equation 1 is the understanding that F would change sign (that is, friction would reverse its direction of action) if u were to change sign. A detailed specification of F is provided in the section on "Constitutive Equations," below.

Conservation of Mass of Solid Plug

Mass change of the solid plug depends on the rate of mass accretion at the base of the plug, ρB, and the rate of mass loss at the surface of plug due to erosion, $\rho_r E$, where B is the volumetric rate of magma conversion to solid rock and E is the volumetric erosion rate of the plug surface. Magma solidification may involve a change in mass density from ρ to ρ_r. Summing these effects yields the mass-conservation equation

$$\frac{dm}{dt} = \rho B - \rho_r E = \kappa, \qquad (2)$$

where κ is a convenient shorthand for $\rho B - \rho_r E$. For the sake of simplicity, κ is assumed constant, although this assumption is readily relaxed in numerical analyses if warranted. With constant κ, equation 2 yields the explicit solution

Table 1. Definitions of mathematical symbols.

Symbol	Dimensions	Definition
A	L^2	Horizontal cross-sectional area of base of plug
B	L^3/T	Volumetric rate of magma solidification at base of plug
C	M/T	Dimensional measure of rate dependence of plug friction force
c	none	Dimensionless measure of rate dependence of plug friction force
c_1, c_2	none	Arbitrary constants of integration
D	none	Dimensionless parameter summarizing effects of frictional damping
E	L^3/T	Volumetric rate of erosion of surface of plug
F	ML/T^2	Friction force on margins of plug
F_0	ML/T^2	Value of F at static limiting equilibrium
$F(u_0)$	ML/T^2	Value of F at the steady equilibrium extrusion rate u_0
F^*	none	F/F_0
G	none	Dimensionless parameter summarizing effects of gravity
g	L/T^2	Gravitational acceleration
H_{con}	L	Vertical height of magma-filled conduit
H_{plug}	L	Vertical height of extruding solid plug
K	none	Dimensionless parameter summarizing effects of plug mass change
m	M	Plug mass
m_0	M	Static or steady equilibrium value of m
p	M/LT^2	Magma pressure against base of plug
p_b	M/LT^2	Magma pressure at base of conduit
p_i	M/LT^2	Value of p at onset of a stick event
p_0	M/LT^2	Value of p at static limiting equilibrium
p_{ref}	M/LT^2	Reference value of p used in magma compression equation
Q	L^3/T	Volumetric rate of magma influx at base of conduit
R	none	Dimensionless parameter equal to $1-\rho/\rho_r$
R_0	none	Value of R when $\rho = \rho_0$
R^*	none	R/R_0
S	none	Dimensionless parameter summarizing rate dependent plug friction
$\hat{S}$	none	Dimensionless parameter summarizing static plug friction
T	T	Oscillation period
t	T	Time
t_0	T	Natural time scale of oscillations, defined in equation 25
t^*	none	t/t_0
u	L/T	Vertical extrusion velocity
u_0	L/T	Value of u at steady equilibrium
u_{ref}	L/T	Reference value of u used in friction equation
u'	L/T	$u-u_0$
u^*	none	u'/u_0
u_i^*	none	Initial value of u^*
V	L^3	Volume of magma-filled conduit
V_0	L^3	Static or steady equilibrium value of V
V'	L^3	$V-V_0$
V^*	none	V'/V_0

Table 1. Definitions of mathematical symbols.—Continued

Symbol	Dimensions	Definition
V_i	L^3	Value of V at onset of stick event
W	L^3/T	Parameter defined in equation 53
X	none	Dimensionless parameter defined in equation 44
Y	none	Dimensionless parameter defined in equation 44
Z	none	Dimensionless parameter defined in equation 44
α_1	LT^2/M	Elastic bulk compressibility of magma
α_2	LT^2/M	Elastic compliance of walls of magma-filled conduit
η	M/LT	Magma viscosity
κ	M/T	Rate of change of plug mass
λ	none	Parameter that relates plug weight to boundary normal stress
μ_0	none	Static friction coefficient
ν	none	Dimensionless parameter defined in equation 34
ρ	M/L^3	Bulk density of magma
ρ_0	M/L^3	Value of ρ at static limiting equilibrium
ρ_r	M/L^3	Bulk density of plug rock
ξ	none	Rescaled time variable defined in equation 34

$$m = \kappa t + m_0 \tag{3}$$

where m_0 is the initial value of m.

Conservation of Linear Momentum of Conduit Fluid

Newton's second law for upward motion of magma in the conduit takes a simple form if variations of magma properties and velocity with position are neglected:

$$\rho \frac{dQ}{dt} + Q \frac{d\rho}{dt} = A\left(\frac{p_b - p}{H_{con}} - \rho g - \frac{8\pi\eta}{A^2} Q \right). \tag{4}$$

Here Q is the vertical (upward) volumetric flux of magma, p_b is the magma pressure at the base of the conduit, and η is the magma viscosity. Equation 4 is the fluid-mechanical equivalent of equation 1 and is also equivalent to the Navier-Stokes equation for one-dimensional laminar flow, integrated over the conduit cross-sectional area A and height H_{con}. According to equation 4, upward motion of magma in the conduit is driven by the vertical pressure gradient $(p_b - p)/H_{con}$ and is resisted by the magma unit weight ρg and viscous drag, represented by the last term in the equation. The form of this drag term is inferred from an elementary analysis of Poiseuille flow in a cylindrical conduit, although alternative drag terms (appropriate for other conduit geometries or magma rheologies) could be used without difficulty.

A simplified momentum equation is obtained by assuming that the magma flux Q is independent of time and making the substitution $dQ/dt = 0$ in equation 4. Rearrangement of the resulting equation yields an explicit expression for Q,

$$Q = A \frac{\frac{p_b - p}{H_{con}} - \rho g}{\frac{d\rho}{dt} + \frac{8\pi\eta}{A}}. \tag{5}$$

Equation 5 shows that maintenance of constant Q in the presence of changing H_{con}, p, and ρ (all of which can occur in the context of the SPASM model) can imply that compensating changes occur in p_b and/or η. The model assumes that such compensating changes may indeed occur, but it does not evaluate such changes explicitly. A complete evaluation could be accomplished by using equation 4 together with a mass-conservation equation (see below) to model the dynamics of transient magma flow in the conduit (for example, Melnik and Sparks, 2002). However, such a model also requires specification of a basal boundary condition (for example, magma-chamber pressure) to drive magma inflow. Any such specification involves assumptions that are arbitrary, and the SPASM model minimizes use of arbitrary assumptions by specifying a constant basal magma influx Q.

Conservation of Mass of Conduit Fluid

The mass of the fluid magma in the conduit is ρV, where V is the conduit volume. Changes in ρV depend not only on changes in ρ and V but also on the influx of fluid mass at the

base of the conduit ρQ and the loss of fluid mass at the top of the conduit ρB, which results from solidification at the base of the solid plug. These phenomena are summarized by the fluid mass-conservation equation

$$\rho \frac{dV}{dt} + V \frac{d\rho}{dt} = \rho(Q - B). \quad (6)$$

Both Q and B are treated as constants.

Constitutive Equations

Although the conservation equations for Q and m reduce to the explicit forms shown above, the remaining two conservation equations (1 and 6) contain four dependent variables, u, p, V, and ρ and an as-yet-unspecified friction force F. Thus, three constitutive equations must be specified to attain mathematical closure.

Magma Compressibility

The first constitutive equation defines the compressibility of the fluid magma α_1 as

$$\alpha_1 = \frac{1}{\rho}\frac{d\rho}{dp}, \quad (7)$$

and integration of equation 7 yields $\rho = \rho_0 \exp[\alpha_1(p - p_{ref})]$, where ρ_0 is the magma bulk density at a reference pressure p_{ref}. Combination of equation 7 with the chain rule $d\rho/dt = (d\rho/dp)(dp/dt)$ yields an equation that relates magma density change to pressure change:

$$\frac{d\rho}{dt} = \alpha_1 \rho \frac{dp}{dt}. \quad (8)$$

Below, this equation is used to replace density derivatives with pressure derivatives where advantageous.

Conduit Compliance

A second constitutive equation defines the bulk elastic compliance of the conduit walls α_2 as

$$\alpha_2 = \frac{1}{V}\left[\frac{dV}{dp}\right]_0, \quad (9)$$

where the subscript 0 denotes conduit volume change under a condition of zero plug velocity (u=0) and zero plug accretion (B=0). The utility of equation 9 is increased by embedding the equation in a definition of the total rate of conduit volume change that occurs when u and B are nonzero,

$$\frac{dV}{dt} = A\,u - \frac{\rho}{\rho_r} B + \left[\frac{dV}{dt}\right]_0. \quad (10)$$

Here again, the subscript 0 denotes the rate of volume change that would exist if u=0 and B=0, whereas the terms Au and $(\rho/\rho_r)\,B$ describe conduit volume change due to upward plug motion and basal plug accretion, respectively. The factor ρ/ρ_r accounts for the influence of density change from ρ to ρ_r during magma solidification at the volumetric rate B.

To obtain a "systemic" constitutive equation for total conduit volume change, equation 9 is embedded in equation 10 by using the chain rule $[dV/dp]_0 = [dV/dt]_0 / (dp/dt)$, yielding

$$\frac{dV}{dt} = A\,u - \frac{\rho}{\rho_r} B + \alpha_2 \frac{dp}{dt} V. \quad (11)$$

The volume change described by equation 11 includes both an irreversible component and a reversible (elastic) component.

Plug Boundary Friction

The final constitutive equation defines the friction force F that acts where the plug contacts the conduit walls. This friction results from shearing of gouge, discussed briefly above in the section on "Gouge Properties" and in detail by Moore and others (this volume, chap. 20). Because friction might potentially exhibit diverse behaviors, and because this diversity has significant ramifications for extrusion dynamics, I represent F with a functional form that is consistent with the key findings of Moore and others (this volume, chap. 20) but that compromises between precision, generality, and simplicity:

$$F = \mathrm{sgn}(u)\, mg\lambda\mu_0 \left[1 + c \sinh^{-1}\left|\frac{u}{u_{ref}}\right|\right]. \quad (12)$$

Here sgn(u) denotes the sign of u and stipulates that the frictional force always opposes motion; μ_0 is a static friction coefficient applicable when u=0; c is a parameter that describes the sign and magnitude of frictional rate dependence; and u_{ref} is a reference velocity that specifies the extent of nonlinearity of rate dependence (fig. 7). In the simplest case, with c=0, equation 12 specifies that the friction force has a constant value $F = F_0 = \mathrm{sgn}(u)\, mg\lambda\mu_0$. If $c \neq 0$ and $u/u_{ref} << 1$, then equation 12 implies that friction depends almost linearly on slip rate ($F \approx \mathrm{sgn}(u)\, mg\lambda\mu_0[1 + c|u/u_{ref}|]$), whereas for $u/u_{ref} >> 1$, equation 12 implies that rate dependence of friction is essentially logarithmic ($F \approx \mathrm{sgn}(u)\, mg\lambda\mu_0[1 + c \ln|2u/u_{ref}|]$) (see Abramowitz and Stegun, 1964, p. 87). This logarithmic dependence mimics behavior observed in the steady sliding experiments of Moore and others (this volume, chap. 20). The fact that nearly logarithmic behavior as well as other styles of frictional behavior may be represented by equation 12 is a significant advantage

in analytical studies. Another advantage is that the equation implies that the maximum friction force is finite at u=0 (that is, $F = F_0 = \pm mg\lambda\mu_0$), whereas purely logarithmic friction rules imply that friction is infinite at u=0.

As specified by equation 12, the friction force F is proportional to the effective normal force on the sides of the plug, $mg\lambda$, where λ is a numerical factor that scales this normal force to the plug weight, mg. This definition implies that the maximum plausible value of λ is about 2 (assuming μ_0~0.5, as shown by the data of Moore and others, this volume, chap. 20), in which case sidewall friction suffices to support the entire plug weight. Realistic values of λ are likely to be considerably smaller than 2 and are dependent on the height of the plug in contact with the conduit walls and on the state of effective stress governing the normal traction on the plug margins. Although the effective stress state is unknown at Mount St. Helens, estimates of λ are constrained by the balance of forces implied by the right-hand side of equation 1 for the case of static limiting equilibrium: $F = F_0 = mg\lambda\mu_0 = pA - mg$. Algebraic rearrangement of this balance shows that λ must satisfy $\lambda = (1/\mu_0)[(pA/mg) - 1]$. Therefore, because the magma pressure p is unlikely to deviate much from lithostatic pressure (for if it did, it would cause hydraulic fracturing or conduit collapse), λ is largely determined by the plug geometry, which determines the plug mass m and basal area A, as well as the depth where p operates.

Although friction described by equation 12 represents both the peak-strength effect and shear-rate effect observed in the experiments by Moore and others (this volume, chap. 20), it includes no provision for the hold-time (or "state evolution") effect also observed in those experiments. In the context of equation 12, inclusion of such evolution would entail making μ_0 a time- or state-dependent quantity. This complication would introduce additional constitutive parameters, but it would add little to understanding the mechanism of regularly occurring drumbeat earthquakes at Mount St. Helens. Therefore, I have chosen to exclude state-evolution effects from the SPASM model.

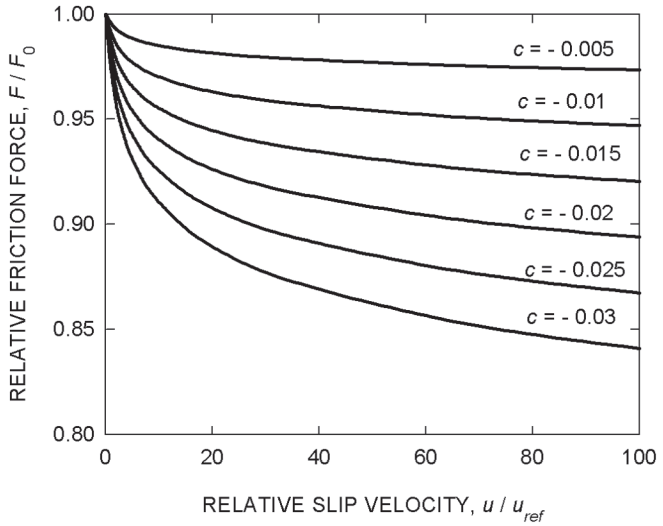

Figure 7. Graph of equation 12, illustrating nonlinear variation of relative friction force as a function of normalized slip rate u/u_{ref} and rate-dependence parameter c. Parameter F_0 is friction force at static, limiting equilibrium, $F_0 = m_0 g\lambda\mu_0$.

Friction represented by equation 12 does include a simple yet fundamental type of state dependence, however. The factor sgn(u) in equation 12 stipulates that the static (zero-velocity) friction force can jump from a positive value $mg\lambda\mu_0$ to a negative value $\geq -mg\lambda\mu_0$ if the extrusion velocity u changes from a positive value to a negative value. If u subsequently becomes positive again, then the friction force again becomes positive. Such jumps ensure that friction opposes motion, and they have great implications for the dynamical behavior of the extruding plug.

Reduced Governing Equations

The equations described above can be reduced to a compact system of three equations governing simultaneous evolution of the dependent variables u, V, and p. In this system the magma density ρ is eliminated as a dependent variable by using equation 8 to replace $d\rho/dt$ in equation 6 with dp/dt and then dividing all terms in the resulting equation by ρ, yielding

$$\frac{dV}{dt} + V\alpha_1 \frac{dp}{dt} = Q - B. \tag{13}$$

Equations 11 and 13 are then combined and rearranged algebraically to obtain explicit equations for $d\rho/dt$ and dV/dt. These two equations accompany the equation of motion obtained by combining equations 2 and 12 with equation 1, thereby forming a system of three first-order differential equations,

$$\frac{du}{dt} = -g + \frac{1}{m_0 + \kappa t}\left[pA - \kappa u - F\,(u/u_{ref})\right], \tag{14}$$

$$\frac{dp}{dt} = \frac{-1/V}{\alpha_1 + \alpha_2}\left[Au + RB - Q\right], \quad \text{and} \tag{15}$$

$$\frac{dV}{dt} = \frac{\alpha_1}{\alpha_1 + \alpha_2}\left[Au + RB - Q\right] + Q - B, \tag{16}$$

where R is a nearly constant coefficient defined by

$$R = 1 - \frac{\rho}{\rho_r} = 1 - \frac{\rho_0}{\rho_r}\exp[\alpha_1(p - p_{ref})]. \tag{17}$$

The system of differential equations (14–16) contains four types of nonlinearities: one involving the quotient Au/V in equation 15, one involving the nonlinear dependence of R on p shown in equation 17, one involving the potential for jumps in F described in the section above on "Plug Boundary Friction," and one involving the dependence of F on $\sinh^{-1}|u/u_{ref}|$ shown in equation 12.

The Forced, Damped Oscillator Equation

The physical implications of the governing equations become clearer when equations 14 and 15 are combined to form a single, second-order equation. Differentiating equation 14 with respect to *t*, employing the chain rule $dF/dt = (dF/du)(du/dt)$, and substituting equation 15 into the resulting equation yields

$$(m_0 + \kappa t)\frac{d^2u}{dt^2} + \left(2\kappa + \frac{dF}{du}\right)\frac{du}{dt} + \left(\frac{A^2}{[\alpha_1 + \alpha_2]V}\right)u = -g\kappa + \frac{A(Q - RB)}{[\alpha_1 + \alpha_2]V}. \quad (18)$$

This equation has a form like that of equations governing behavior of forced, damped oscillators (Kreyszig, 1979, p. 82 ff.), and it implies that the extrusion velocity *u* has a natural tendency to oscillate about equilibrium. This tendency arises from the interplay of plug inertia, an upward "spring force" due to compression of the magma and conduit, and the downward force due to gravity. Oscillations of *u* are complicated by the presence of a time-dependent mass term $m_0 + \kappa t$, variable damping implicit in dF/du, and variable forcing due to the presence of *R* and *V* in the last term of equation 18, as well as by coupling of equation 18 to equations 16 and 17. Of course, equation 18 is strictly valid only insofar as *F* is a continuously differentiable function of *u*, and this restriction must be borne in mind when interpreting solutions of equation 18.

Linearized Dynamics: Analytical Results

Analytical solutions of equation 18 are important for guiding interpretation and numerical solution of the full equation set, 14–16, despite the fact that analytical solutions can be readily obtained only for various special cases. Analytical results also aid identification of diverse eruptive styles that are represented by the governing equations but are difficult to identify through numerical solutions alone.

Static, Steady-State, and Pseudosteady-State Solutions

The most basic special cases involve assumptions about the extrusion velocity *u*. A very simple special case with great physical importance assumes a condition of static limiting equilibrium, in which $u = 0$ and plug boundary friction just suffices to resist the upward force due to magma pressure. This case also assumes that the plug mass is constant (that is, $\kappa = 0$, $m = m_0$) and that the magma influx rate *Q* and basal accretion rate *B* are zero. These assumptions lead to the static equilibrium solution,

$$u = 0 \qquad p = p_0 = \frac{m_0 g + F_0}{A} \qquad V = V_0, \quad (19)$$

which satisfies equations 14–16 as well as 18. Here p_0 is the limiting equilibrium magma pressure at the base of the plug, F_0 is the friction force at static limiting equilibrium, $F_0 = m_0 g \lambda \mu_0$, and V_0 is an arbitrary but constant conduit volume.

An equally important special case assumes that the plug mass is constant ($\kappa = 0$, $m = m_0$) but that volumetric rate of basal plug accretion and volumetric rate of magma influx are finite and equal (*B*=*Q*). These conditions lead to an exact steady-state solution satisfying equations 14–16 as well as 18,

$$u = u_0 = \frac{Q - R_0 B}{A} \qquad p = \frac{m_0 g + F(u_0)}{A} \qquad V = V_0 \quad (20)$$

in which u_0 is the steady-state upward plug velocity, $F(u_0)$ is the steady-state friction force, $F(u_0) = m_0 g \lambda \mu_0 [1 + c \sinh^{-1}(u_0 / u_{ref})]$, and R_0 is a constant value of *R* that applies when $\rho = \rho_0$ (that is, $R_0 = 1 - (\rho_0 / \rho_r)$). The equation group 20 represents dynamic equilibrium of the steadily ascending magma-plug system, whereas transient states represent departures from this equilibrium. Below, analyses of these departures show that steady states can be stable in some circumstances and unstable in others.

In addition to the exact steady state described by equation group 20, pseudosteady states can exist in which the extrusion velocity *u* remains constant but the magma pressure *p* increases or decreases as the plug mass evolves according to $m = m_0 + \kappa t$. A pseudosteady-state solution that satisfies equations 14–16 and 18 is

$$u = \frac{Q - R_0 B}{A} - \frac{\kappa g(\alpha_1 + \alpha_2)V}{A^2} \qquad p = \frac{m_0 g + F(u)}{A} + \frac{\kappa(gt + u)}{A}$$

$$V = \frac{A(Q - B)}{\kappa g \alpha_1}. \quad (21)$$

Existence of this pseudosteady state requires that $B \neq Q$ and that *R* changes negligibly as *p* evolves. Despite these restrictions, the state described by equation group 21 has physical significance because it implies that essentially steady extrusion may occur in the presence of evolving plug mass and magma pressure, and it has mathematical significance because it provides a check on numerical results reported later in this paper. Additional pseudosteady states may, of course, exist if values of other parameters (for example, F_0, *A*, α_1, α_2) evolve, but such evolution is not addressed explicitly in this paper.

Linear Approximation of Transient States

Analysis of transient states is facilitated by linearization. As a first step, the dependent variables *u* and *V* in equation 18 are decomposed into sums of the steady-state values, defined in equation group 20, and transient deviations from steady state, denoted by primes:

$$u = u_0 + u'(t) \qquad V = V_0 + V'(t). \tag{22}$$

Substitution of equation group 22 into 18 and elimination of terms that sum to zero yields a simplified, but still nonlinear, version of equation 18 that describes the behavior of transient deviations. One linearization of this equation results from the assumption that magma density changes are small in comparison to the steady-state density, which enables *R* to be approximated by its steady-state value $R_0 = 1-(\rho_0/\rho_r)$. A second linearization involves the assumption that deviations in the magma-conduit volume are small in comparison to its steady-state volume (that is, $V'/V_0 << 1$). Then neglect of small terms involving V'/V_0 decouples equation 18 from 16 and removes the associated nonlinearity. These two linearizations generally have little effect on model predictions because they involve physical effects that are typically very subtle.

The most significant linearization involves approximation of dF/du in equation 18. If *u* remains positive, an exact, nonlinear expression for dF/du follows from the definition of *F* in equation 12 and can be written as (see Abramowitz and Stegun, 1964, p. 88)

$$\frac{dF}{du} = \frac{m_0 g \lambda \mu_0 c}{u_{ref}} \left[1 + \left(\frac{u}{u_{ref}} \right)^2 \right]^{-1/2}. \tag{23a}$$

Substituting $u = u_0 + u'$ in equation 23a and simplifying the result algebraically yields an approximation of 23a that is valid if velocity deviations from steady state are sufficiently small that $u'/u_0 << 1$ and $u'/u_{ref} << 1$:

$$\frac{dF}{du} \approx \frac{m_0 g \lambda \mu_0 c}{u_{ref}} \left[1 + \left(\frac{u_0}{u_{ref}} \right)^2 \right]^{-1/2} = C. \tag{23b}$$

Here *C* is a constant with the same sign as *c* but with dimensions of mass/time. If friction is rate independent, then *C*=0, whereas *C*>0 indicates rate-strengthening friction and *C*<0 indicates rate-weakening friction.

The linearized form of equation 18 results from making the substitutions shown in equations 21 and 23b and assuming $R = R_0$, $V'/V_0 << 1$, and $u'/u_0 << 1$, which yields

$$\left(1 + \frac{\kappa t}{m_0} \right) \frac{d^2 u'}{dt^2} + \left(\frac{2\kappa + C}{m_0} \right) \frac{du'}{dt} + \left(\frac{A^2}{m_0 V_0 [\alpha_1 + \alpha_2]} \right) u' = -\frac{g\kappa}{m_0}. \tag{24}$$

Except for the plug mass-growth factor $\kappa t/m_0$, all coefficients in equation 24 are constant, a property that facilitates analysis.

Natural Period of Oscillations

The form of equation 24 implies that if $\kappa = 0$ (that is, the plug mass is constant), then u' will oscillate freely with constant period $T = 2\pi t_0$, where t_0 is the natural time scale implied by the reciprocal of the coefficient that precedes u' in equation 24:

$$t_0 = \frac{[m_0 V_0 (\alpha_1 + \alpha_2)]^{1/2}}{A}. \tag{25}$$

This result is demonstrated more formally in the section on "Solution for Undamped Free Oscillations" below, but *T* and the time scale t_0 are introduced here as a basis for normalization of equation 24 and a first comparison of *T* and the typical interval between repetitive drumbeat earthquakes at Mount St. Helens. To facilitate this comparison, equation 25 is recast in a special form that is appropriate if the magma conduit and plug are approximated as right cylinders (not necessarily circular) with cross-sectional areas *A* and heights H_{con} and H_{plug}, respectively. In this case the oscillation period $T = 2\pi t_0$ can be expressed as

$$T = 2\pi [(\alpha_1 + \alpha_2) \rho_r H_{con} H_{plug}]^{1/2}. \tag{26}$$

A graph of equation 26 for the values H_{con} = 8 km and ρ_r = 2,000 kg/m^3 is depicted in figure 8. The graph shows how the free oscillation period *T* varies as a function of the plug height H_{plug} and lumped compressibility $\alpha_1+\alpha_2$. For reasonable values of H_{plug} and $\alpha_1+\alpha_2$, the predicted *T* has values that range from about 10 s to several minutes. The similarity of these values to the observed recurrence period of drumbeat earthquakes during the 2004–5 eruption of Mount St. Helens helps support the hypothesis that the drumbeats were associated with oscillations of the extrusion rate *u*.

Normalized Oscillator Equation and Dimensionless Parameters

The quantity t_0 defined in equation 25 provides the appropriate time scale for normalization of equation 24, and this normalization leads to identification of the dimensionless parameters that control the linearized dynamics of the magma-plug system. Substitution of the normalized time $t^* = t/t_0$ and normalized velocity deviation $u^* = u'/u_0$ into equation 24 reduces the equation to

$$(1+Kt^*) \frac{d^2 u^*}{dt^{*2}} + (2K+GS) \frac{du^*}{dt^*} + u^* = -KG \tag{27}$$

in which *K*, *S*, and *G* are dimensionless parameters defined as

$$K = \frac{\kappa t_0}{m_0}, \tag{28}$$

$$S = \frac{C u_0}{m_0 g}, \quad \text{and} \tag{29}$$

$$G = \frac{g t_0}{u_0}. \tag{30}$$

It is also useful to define a dimensionless damping factor D, which is half the coefficient in the second term of equation 27:

$$D = \frac{1}{2}(2K + GS) = \frac{t_0}{m_0}\left(\kappa + \frac{C}{2}\right) \tag{31}$$

If K=0, this damping factor plays a role like that of damping factors in textbook examples of linear oscillators, and D=1 constitutes critical damping (for example, Kreyszig, 1979, p. 82 ff.). This interpretation changes only subtly for cases with $K \neq 0$, as shown below.

A complete assessment of the magnitudes of the dimensionless parameters defined above is provided in the section on "Normalized Nonlinear Equations and Control Parameters" below, but for present purposes it suffices to note that typical magnitudes of K, G, and S imply that a satisfactory approximation of equation 27 commonly results from neglecting the plug growth term Kt^* as well as the effect of K on D. An even simpler but still relevant approximation is obtained by setting both K and S equal to 0 in equation 27. On the other hand, because solutions of equation 27 for nonzero values of these parameters imply diverse eruptive behaviors, which can differ qualitatively as well as quantitatively, I analyze the full spectrum of these behaviors before considering numerical solutions of the nonlinear system of equations 14–16.

Solution for Undamped Free Oscillations

For the case in which K=0 and S=0 (implying constant plug mass and constant plug-margin friction), equation 27 reduces to an elementary second–order equation describing undamped, free oscillations of the plug velocity. In this case the simplest nontrivial solution of equation 27 is

$$u^* = u_i^* \cos t^*, \tag{32}$$

which obeys the initial conditions $u^* = u_i^*$ and $du^*/dt^* = 0$. This solution demonstrates that the natural period of the plug's velocity oscillations is $T = 2\pi t_0$, as inferred in the section on "Natural Period of Free Oscillations" above. According to equation 32, sinusoidal oscillations with period T and amplitude u_i^* continue forever if an initial disturbance with magnitude u_i^* causes them to begin, provided that K=S=0.

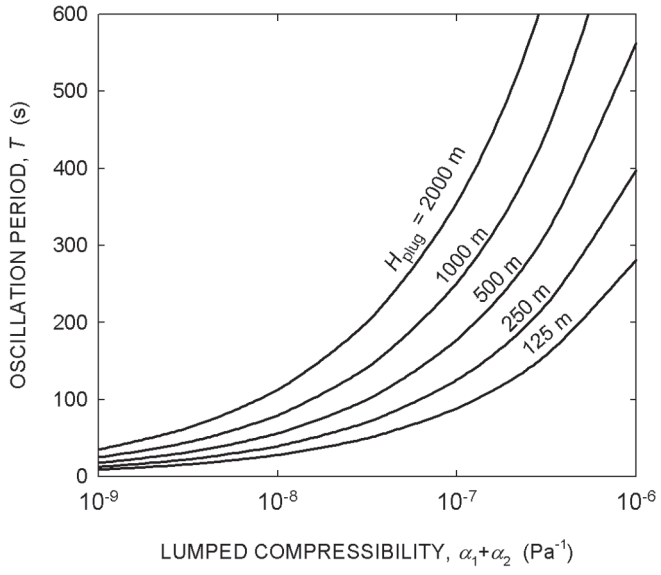

Figure 8. Graph of equation 26, illustrating predictions (from linearized theory) of variation of oscillation period T as a function of lumped compressibility $\alpha_1 + \alpha_2$ and plug height H_{plug}.

Solutions for Damped Free Oscillations—Stability of Quasi-Steady Extrusion

Another class of solutions of equation 27 exists if K=0 but $S \neq 0$. Physically, these conditions imply that the plug mass is constant $S \neq 0$ and that plug-margin friction depends linearly on the extrusion rate. In such cases the behavior of solutions depends on the value of D(= S/2) relative to the transition value D=0 and critical values D=±1, as summarized in table 2. In all cases the solutions imply stable eruptive behavior if D>0 (that is, if rate-strengthening friction exists), because u^* decays with time essentially like e^{-Dt^*}. On the other hand, if D<0 (that is, if rate-weakening friction exists), solutions containing the factor e^{-Dt^*} indicate unstable growth of u^*. The instability can be manifested as either runaway acceleration or oscillations that grow with time, as shown by the solutions listed in table 2.

The solutions listed in table 2 can also be used to infer whether the steady eruptive state represented by equation group 20 is physically accessible from an initial static state that exists before the onset of a volcanic eruption. For all cases with D>0, transient deviations in velocity (u^*) decay toward zero as time proceeds, implying that any transient state will eventually give way to a steady state. On the other hand, for cases in which D<0, dynamic steady states are inaccessible from an initial static state, because any transient motion grows without bound as time proceeds. Of course, this simple picture can change if $K \neq 0$ or if friction is nonlinear, as described in the section on "Nonlinear Dynamics: Numerical Results" below.

Solution for Damped, Forced Oscillations—Effects of Plug Growth on Extrusion Stability

The most complicated solutions of equation 27 apply to cases in which the plug mass changes with time such that $\kappa \neq 0$ and none of the parameters K, S, and G is zero. For such cases, solutions can be obtained by a multistep process that involves a simultaneous change of dependent and independent variables to transform equation 27 into Bessel's differential

Table 2. General solutions of equation 27 for cases with K=0 and $D=S/2$. All solutions contain arbitrary constants, c_1 and c_2, which are constrained by specifying initial conditions.

$\lvert D\rvert$	General solution of equation 27	Type of behavior
0	$u^* = c_1 \sin t^* + c_2 \cos t^*$	Undamped oscillations with constant amplitude
>0 but <1	$u^* = [c_1 \cos(t^*\sqrt{1-D^2}) + c_2 \sin(t^*\sqrt{1-D^2})]\ e^{-Dt^*}$	Underdamped oscillations; unstable growth if D<0
1	$u^* = (c_1 + c_2 t^*)\, e^{-Dt^*}$	Critically damped oscillation; unstable growth if D<0
>1	$u^* = c_1 e^{(-D+\sqrt{D^2-1})t^*} + c_2 e^{(-D-\sqrt{D^2-1})t^*}$	Overdamped, no oscillations; unstable growth if D<0

equation (appendix 1). Transformation of the well-known Bessel-equation solution back to the original variables u^* and t^* then yields the general solution

$$u^* = -KG + \frac{\xi^v}{4}\left[c_1 J_v(\xi) + c_2 Y_v(\xi)\right], \tag{33}$$

in which

$$v = \frac{K-2D}{K} \qquad \xi = 2\sqrt{\frac{1+Kt^*}{K^2}}. \tag{34}$$

Here c_1 and c_2 are arbitrary constants, and J_v and Y_v are Bessel functions of the first and second kind, of order v (see Abramowitz and Stegun, 1964). Equation 33 describes diverse behaviors, partly analogous to those summarized in table 2. However, oscillations described by equation 33 have periods as well as amplitudes that evolve with time.

The relation between the solution for $K\neq 0$ (equation 33) and the solutions for K=0 (table 2) has important physical implications. The relation is clarified by considering asymptotic approximations of J_v and Y_v that are valid for $\xi >> 1$. (The condition $\xi >> 1$ implies $t^* >> K - 1/K$, a criterion that is typically satisfied as time proceeds if K>0. If K<0, the criterion will not be satisfied as time proceeds, and equation 33 then implies that a singularity develops in which $u^* \to \infty$. Physically, this singularity represents a "catastrophe" in which the plug mass reaches zero, liquid magma reaches the surface, and the governing equations no longer apply.) For $\xi >> 1$ the Bessel function approximations are (Abramowitz and Stegun, 1964, p. 364)

$$J_v(\xi) \approx \sqrt{\frac{2}{\pi\,\xi}}\ \cos(\xi - v\pi/2 - \pi/4), \quad \text{and} \tag{35}$$

$$Y_v(\xi) \approx \sqrt{\frac{2}{\pi\,\xi}}\ \sin(\xi - v\pi/2 - \pi/4). \tag{36}$$

Substituting these approximations into equation 33 and collecting terms containing powers of ξ shows that, over time, u^* decays or grows according to

$$u^* \propto \left(\frac{1+Kt^*}{K^2}\right)^{1/4 - D/K}. \tag{37}$$

The exponent $1/4 - D/K$ in equation 37 plays a physical role analogous to that of $-D$ in solutions with K=0 (table 2). The physical meaning of equation 37 becomes clearer if equations 29 and 31 are used to express the exponent in terms of physical parameters, yielding

$$u^* \propto \left(\frac{1+Kt^*}{K^2}\right)^{-\frac{1}{2}\left(\frac{3}{2}+\frac{C}{\kappa}\right)}. \tag{38}$$

The exponent in equation 38 shows that oscillations in u^* will decay or grow depending on whether the criterion

$$\frac{C}{\kappa} > -\frac{3}{2} \tag{39}$$

is satisfied. Several classes of behavior are implied by this result and are summarized in table 3.

The chief physical implication of the results summarized in table 3 is that extrusion stability can depend on a tradeoff involving the rate dependence of the frictional resisting force and the rate of change of plug mass. Stable eruptive behavior can occur in the presence of rate-weakening friction (C<0) if the plug mass increases at a sufficient rate. This behavior contrasts with that of a system with constant plug mass, which necessarily exhibits unstable behavior if C<0 and, therefore, D<0 (table 2). Conversely, unstable behavior can occur in the presence of rate-strengthening friction (C>0) if the plug mass decreases at a sufficient rate.

Although further inferences can be drawn from the analytical results summarized by equations 38 and 39, for present purposes it

Table 3. Summary of behavior of equation 33, which is general solution of equation 27 for cases with changing plug mass ($K \neq 0, \kappa \neq 0$).

[Behavior for both rate-strengthening friction ($C > 0$) and rate-weakening friction ($C < 0$) is summarized.]

κ	C	Behavior of equation 33
$\kappa = -(2/3)C$	$C = -(3/2)\kappa$	Undamped, constant-amplitude oscillations
$\kappa > 0$	$C > 0$	Oscillations necessarily decay toward a steady state
$\kappa > 0$	$C < 0$	Oscillations grow if $\kappa < -(2/3)C$ and decay if $\kappa > -(2/3)C$
$\kappa < 0$	$C > 0$	Oscillations grow if $\kappa < -(2/3)C$ and decay if $\kappa > -(2/3)C$
$\kappa < 0$	$C < 0$	Behavior becomes singular

is more useful next to consider numerical solutions of the nonlinear equation set 14–16. Nonlinearities produce important effects that are not revealed by analytical results that strictly apply only when transient disturbances are small (that is, $u'/u_0 << 1$).

Nonlinear Dynamics: Numerical Results

Results of the linear theory point to several questions to be addressed through numerical solution of the nonlinear system of equations 14–16. Do the bounds of stable versus unstable eruptive behavior and character of oscillatory eruptive behavior change when nonlinearities exist? More specifically, can nonlinearities result in stick-slip instabilities like those inferred to produce drumbeat earthquakes at Mount St. Helens? What controls the magnitude and frequency of stick-slip events? Can such events occur repeatedly (that is, forever) until some attribute of the system changes? Can evolution of stick-slip periods and amplitudes yield inferences about evolution of system properties? Do complications such as plug mass change have significant effects? How sensitive are the system's dynamics to disequilibrium initial conditions? (Although the linear theory assumes that departures from equilibrium are always small, nature imposes no such constraint, and volcanic eruptions necessarily begin in disequilibrated states.)

Normalized Nonlinear Equations and Control Parameters

Guidance for investigating the behavior of numerical solutions comes from identification of dimensionless control parameters and their likely magnitudes. Behavior of the nonlinear equations is governed partly by the same dimensionless parameters that govern linearized behavior, but additional parameters also play a role. The additional control parameters are identified by normalizing the nonlinear system of first-order equations 14–16 through use of dimensionless variables defined as $u^* = u/u_0$, $p^* = p/p_0$, $V^* = V/V_0$, $t^* = t/t_0$.

Substituting these variables into equations 14–16 yields the normalized system

$$\frac{du^*}{dt^*} = -G + \frac{1}{1+Kt^*}\left[G(1+\hat{S})p^* - Ku^* - G\hat{S}F^*\right], \quad (40)$$

$$\frac{dp^*}{dt^*} = \frac{-1/V^*}{G(1+\hat{S})}\left[u^* - 1 + Z(R^* - 1)\right], \quad \text{and} \quad (41)$$

$$\frac{dV^*}{dt^*} = X\left[u^* - 1 + Z(R^* - 1)\right] + Y. \quad (42)$$

Here, G and K are dimensionless parameters defined exactly as in the linear model (that is, in equations 28 and 30). The dimensionless parameter $\hat{S}$ is related to S defined in the linear model (that is, in equation 29), but its definition is somewhat simpler because it involves F_0 rather than the derivative $C = dF/du$:

$$\hat{S} = \frac{F_0}{m_0 g} = \lambda\mu_0. \quad (43)$$

The dimensionless parameters X, Y, and Z have no analog in the linear model and are defined as

$$X = \frac{\alpha_1 m_0 u_0}{A t_0} \qquad Y = \frac{t_0(Q-B)}{V_0} \qquad Z = \frac{R_0 B}{u_0 A}. \quad (44)$$

The variables R^* and F^* in equations 40–42 are normalized versions of the density variable R defined in equation 17 and the friction force F defined in equation 12:

$$R^* = \frac{R}{R_0} = \frac{1 + (R_0 - 1)\exp\left[XG(1+\hat{S})(p^* - 1)\right]}{R_0}, \quad (45)$$

$$F^* = \frac{F}{F_0} = \mathrm{sgn}(u^*)\left(1 + c\sinh^{-1}[u^*(u_0/u_{ref})]\right). \quad (46)$$

In the nonlinear version of the SPASM model, equations 45 and 46 must be satisfied simultaneously with equations 40–42.

Plausible ranges of the values of the dimensionless parameters in equations 40–46 for the 2004–5 eruption of Mount St. Helens are listed in table 4. The tabulated values imply that some of the terms in equations 40–46 will have little influence on numerical results. For example, relevant values of the denominator $G(1+\hat{S})$ on the right-hand side of equation 41 are undoubtedly very much greater than 1, implying that p^* will remain close to its static equilibrium value $p^* = 1$. This inference, together with the inference that $X<<1$ (table 4), implies that the argument of the exponential function in equation 45 will remain close to zero, despite the large probable value of $G(1+\hat{S})$. Therefore, $R^*=1$ is typically a good approximation of equation 45, and this approximation implies that the term $Z(R^*-1)$ in equations 41 and 42 will have only subtle effects. Similarly, the term Y in equation 42 will have subtle effects because $Y<<1$ (table 4). As a basis for prioritizing investigations, then, it is reasonable to assume initially that $Y=Z=0$.

With these simplifications in mind, equation 40 can be differentiated and combined with equation 41 to obtain a second-order equation, which can also be obtained through normalization of the original oscillator equation 18. For the case in which $R^*=1$ is a good approximation, the complete system of normalized nonlinear governing equations thereby reduces to

$$\left(1+Kt^*\right)\frac{d^2u^*}{dt^{*2}}+(2K+GS)\frac{du^*}{dt^*}+\frac{1}{V^*}u^*=\frac{1}{V^*}-K\,G, \quad \text{and} \tag{47}$$

$$\frac{dV^*}{dt}=X(u^*-1). \tag{48}$$

Note that S rather than $\hat{S}$ appears in equation 47, and that the entire set of dimensionless parameters has collapsed to K, G, X, and S in equations 47 and 48. Moreover, the values of K and X are typically much smaller than 1 (table 4), and the effects of terms containing K and X are therefore apt to be modest. On this basis, computational investigations aimed at illuminating the physics represented by the SPASM model can focus principally on the effects of G and S, secondarily on the effects of K, and lastly on the effects of X, Y, and Z.

The strategy of focusing primarily on effects of G and S reduces the need to explore a large, multidimensional parameter space numerically, and it parallels development of the linearized theory, in which D emerged as the key control parameter. Indeed, D defined in the linearized theory applies also to the nonlinear model, provided that D is viewed as a numerical index rather than a constant damping factor. For this purpose it is useful to define the index D as the value applicable when the slip rate equals the steady equilibrium rate ($u = u_0$):

$$D_{u=u_0}=\frac{1}{2}\,(2K+GS)= \tag{49}$$
$$\frac{1}{2}\left(\frac{2\kappa t_0}{m_0}+c\lambda\mu_0\,\frac{gt_0}{u_{ref}}\left[1+\left(\frac{u_0}{u_{ref}}\right)^2\right]^{-1/2}\right).$$

This equation is simply an algebraically expanded version of the definition given in equation 31, and I employ this definition of D to index numerical results.

It is also noteworthy that for cases in which K=0 and $u_0/u_{ref} >> 1$, equation 49 reduces to the simplified form

$$D\approx\frac{1}{2}\left(c\lambda\mu_0\,\frac{gt_0}{u_0}\right), \tag{50}$$

which is commonly a satisfactory approximation. In the sparest distillation of the nonlinear SPASM model, then, numerical results can be expected to depend primarily on D as defined in equation 50, which in turn depends only on c, λ, and μ_0 if the equilibrium extrusion rate u_0 and oscillation time scale t_0 are fixed.

Computational Method

Numerical solutions were obtained by using a standard fourth-order Runge-Kutta method described by Press and others (1986). To implement the Runge-Kutta algorithm, a double-precision FORTRAN program was written and executed on a personal computer with a 2.26-GHz processor. Constant time steps were used to generate all solutions and were typically 0.0001 to 0.01 s. Although some exploratory computations required hours of CPU time, no computations reported in this paper required more than several minutes of CPU time when using this constant-time-step approach.

The accuracy of numerical solutions was checked against exact analytical solutions for simple linear cases with constant values of D and K (table 2 and equation 33). For nonlinear cases, some aspects of numerical solutions were checked analytically by exploiting the fact that the governing equations 14–16 yield nearly exact solutions for p and V for the special case in which u = 0. These solutions assume that $R = R_0$, and they have the form

$$V=V_i+Wt, \quad \text{and} \tag{51}$$

$$p=p_i+\frac{Q-R_0B}{(\alpha_1+\alpha_2)W}\,\ln\left[1+\frac{W}{V_i}t\right], \tag{52}$$

where

$$W=\frac{\alpha_1}{\alpha_1+\alpha_2}\,\left[R_0B-Q\right]+Q-B. \tag{53}$$

Here V_i and p_i are the values of V and p at the beginning of any "stick" episode with u=0. The duration of stick episodes, T_{stick}, may be calculated by solving equation 52 for t while setting p equal to the static limiting equilibrium pressure p_0 necessary to trigger any slip episode,

$$T_{stick}=\frac{V_i}{W}\left[\exp\left(\frac{(p_0-p_i)(\alpha_1+\alpha_2)\,W}{Q-R_0B}\right)-1\right]. \tag{54}$$

Table 4. Plausible values of SPASM model parameters applicable to the quasi-steady dome-building eruption of Mount St. Helens, 2004–2005.

[Derived dimensionless parameters determine model behavior and are formed from combinations of physical parameters.]

Parameter	Units	Value(s)	Comments on value(s)
Specified physical parameters			
A	m^2	30,000	Calculated using Q/u_0 and values tabulated here
B	m^3/s	0–10	Cannot differ greatly from Q
c	none	-0.01–0.01	Inferred from results of testing by Moore and others, (this volume, chap. 20)
C	kg/s	$\lvert C \rvert < 5\times10^{13}$	Calculated using equation 23 and values tabulated here
g	m/s^2	9.8	Typical value at Earth's surface
m_0	kg	5×10^9–7×10^{10}	Inferred from plug heights 100–1,000 m and A and ρ_r tabulated here
Q	m^3/s	1–2	Inferred from photogrammetric measurements of dome growth
R_0	none	-0.5–0.5	Calculated from typical values of ρ_0 and ρ_r tabulated here
t_0	s	0.4–150	Calculated from equation 25 and other values tabulated here
u_0	m/s	2×10^{-5}–7×10^{-5}	Inferred from measured linear extrusion rate
u_{ref}	m/s	7×10^{-8}–7×10^{-5}	Smaller than u_0 if friction rate-dependence is nonlinear
V_0	m^3	3×10^6–3×10^8	Inferred from 8 km conduit height and conduit radii 10–100 m
α_1	Pa^{-1}	10^{-8}–10^{-6}	Typical values for silicic magma with 1–50 vol percent bubble content
α_2	Pa^{-1}	$\leq 10^{-9}$	Typical values for fractured rock
κ	kg/s	$\lvert \kappa \rvert < 4{,}000$	Exceptions may occur during dome-collapse events
λ	none	0.1–1	Inferred from plug geometry and plausible effective stress states
μ_0	none	0.4–0.5	Inferred from results of testing by Moore and others, (this volume, chap. 20)
ρ_0	kg/m^3	1,200–2,400	Typical values for silicic magma with 1–50 vol percent bubble content
ρ_r	kg/m^3	1,600–2,400	Inferred from measurements on dome-rock specimens
Derived dimensionless parameters			
D	none	-10^7–10^7	Influence of D can be very significant
G	none	6×10^4–2×10^7	Influence of G is very significant
K	none	$\lvert K \rvert \leq 10^{-4}$	Influence of K is subtle except in event of abrupt dome collapse
S	none	-7–7	Influence of S is significant
$\hat{S}$	none	-0.5–0.5	Influence of $\hat{S}$ is significant if multiplied by G
X	none	4×10^{-4}–8×10^{-10}	Influence of X is subtle except perhaps where multiplied by G
Y	none	$\lvert Y \rvert \leq 10^{-4}$	Influence of Y is subtle
Z	none	$\lvert Z \rvert < 0.5$	Influence of Z may be significant, contingent on value of R^*

This equation is useful for checking computational results, and it also has a significant physical implication: the duration of stick episodes increases exponentially with $p_0 - p_i$. From this result it may be inferred that plug displacements during slip events also increase exponentially with $p_0 - p_i$, because the average extrusion velocity is fixed (as given by equation 20), and slip-event magnitude must therefore increase in proportion to stick duration. Although strict validity of equations 52 and 54 rests on the assumption that $R = R_0$, computations that do not employ this assumption show that, nonetheless, equations 52 and 54 generally provide good predictions.

Computational Results

Only a small number of computational solutions are presented here, but hundreds of additional solutions were computed and examined. Results chosen for presentation

highlight a range of physical effects that appear particularly important for understanding the origin of drumbeat earthquakes at Mount St. Helens. To a lesser degree, results were also chosen to illustrate the spectrum of behaviors possible within the framework of the SPASM model.

Behavior with *D* Close to Zero

The most basic nonlinear features of solutions appear even when departures from linear behavior are slight. In particular, stick-slip cycles develop in any case in which $D<0$, provided that a jump in F is imposed at $u=0$. Figure 9 illustrates this behavior for a case in which $D=-0.01$, $B=Q$, and F depends linearly on u (that is, $F=\mathrm{sgn}(u)\,m_0 g\lambda\mu_0[1+c\,|u/u_{ref}|]$). The small value of D results from use of an unusually small value of λ, $\lambda=0.01$; physically, this value implies that frictional resistance and the damping it produces are small. The computation also used the initial conditions $u=Q/A$, $V=V_0$, and $p=p_0$, which imposed a slightly perturbed initial magma pressure (because the static equilibrium pressure p_0 slightly exceeds the steady equilibrium pressure) and used the parameter values $K=0$, $Y=0$, $Z=0$, $X=5\times10^{-6}$, $T=10$ s, $\rho_0=\rho_r=2{,}000$ kg/m^3, $m_0=3.6\times10^{10}$ kg, $\mu_0=0.5$, $c=-1.71\times10^{-5}$, and $u_{ref}=0.1(Q/A)=6.66710^{-6}$ m/s. The fact that the value of u_{ref} is significantly smaller than that of the typical extrusion rate (Q/A) implies that effects of rate dependence in the friction rule are important.

Under the conditions described above, the computed extrusion behavior is initially identical to that predicted by the linear analytical theory, and u, p, and V each exhibit exponentially growing sinusoidal oscillations until $u=0$ occurs (at $t\approx$ 27 s in fig. 9). At that time F momentarily changes sign and thereby halts motion of the plug as it starts to descend. This event heralds the end of exponential oscillation growth and the onset of repetitive stick-slip cycles.

In both the sinusoidal and stick-slip cycles shown in figure 9, magma pressure oscillates ¼ cycle out of phase with slip velocity, and conduit volume oscillates ½ cycle out of phase with magma pressure. Although it may seem contradictory that conduit volume decreases as magma pressure increases, this out-of phase response results from conditions at the base of the extruding plug, where solidification and accretion occur continuously at the volumetric rate B, even as plug velocity diminishes to less than the steady-state value $u=Q/A=6.667\times10^{-5}$ m/s. Indeed, as a rough approximation, conduit volume declines whenever the plug extrusion rate is less than the basal accretion rate. The conduit volume also responds elastically to pressure changes, but this effect is typically overshadowed by volume changes associated with plug motion and basal accretion.

Key elements of the solution presented in figure 9 are recast in a phase-plane diagram in figure 10, which shows how pressure deviations from the static equilibrium pressure p_0 vary in concert with velocity deviations from the steady equilibrium velocity Q/A. As portrayed in the phase plane, the initial condition ($u=Q/A$, $p=p_0$, marked I.C. in fig. 10) is unstable. This instability leads to an outwardly diverging clockwise spiral representing simultaneous oscillations of u and p that grow with time. (Note that arrows in phase-plane diagrams throughout this paper point in the direction of advancing time.) When the spiral becomes large enough to encounter the condition $u=0$, divergence ceases and the dynamics become locked in stick-slip limit cycles that repeat endlessly thereafter. If the initial condition is located elsewhere inside the stick-slip limit cycle of figure 10, behavior nonetheless diverges smoothly until locking in the same limit-cycle state. If friction exhibits rate-strengthening rather than

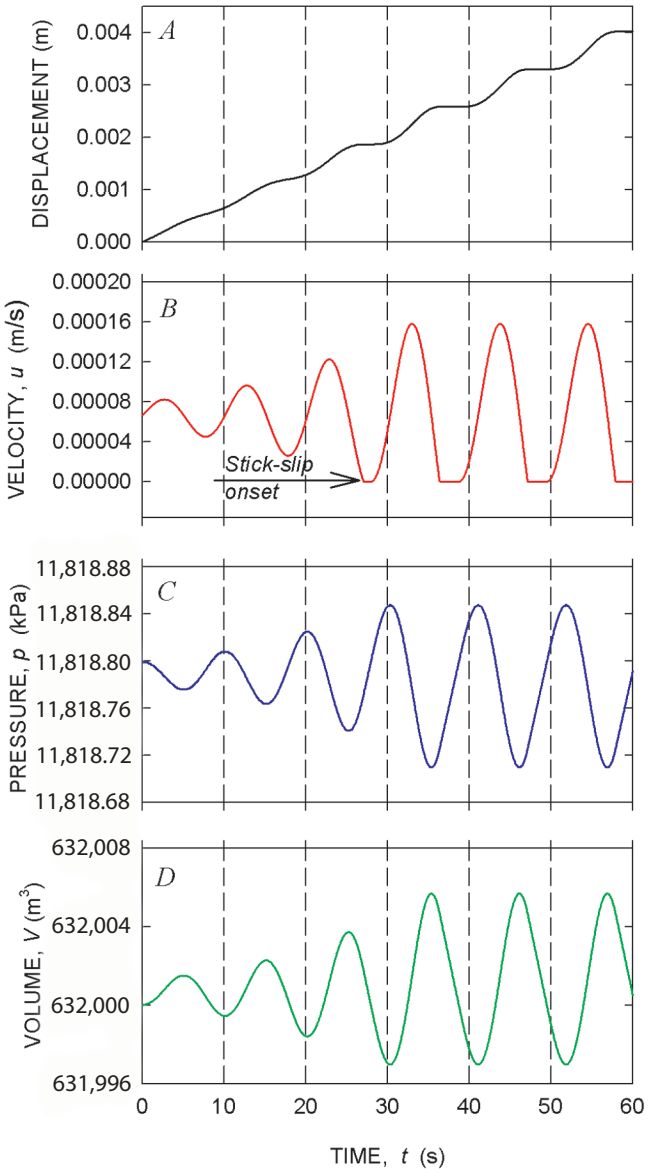

Figure 9. Start-up behavior of solution computed for D = –0.01 with linear rate weakening. Initial condition is $u=Q/A$, $p=p_0$, $V=V_0$. Oscillations of slip velocity (u), magma pressure (p) and conduit volume (V) are sinusoidal and match analytical predictions until $u=0$ occurs and stick-slip behavior begins.

rate-weakening behavior (that is, $D>0$), then behavior converges smoothly to a steady fixed-point equilibrium instead. An analogous fixed-point equilibrium is exhibited by eruption models that assume forces are always balanced (for example, Mastin and others, this volume, chap. 22).

Modification of the behavior depicted in figures 9 and 10 by nonlinearity in the rate-weakening friction rule is illustrated in figures 11 and 12. Initial conditions and parameter values used to generate figures 11 and 12 were the same as those used to generate figures 9 and 10, but the nonlinear friction rule $F = \mathrm{sgn}(u)\, mg\lambda\mu_0[1 + c\sinh^{-1}|u/u_{ref}|]$ was employed. Comparison of figure 11 with figure 9 demonstrates that the most conspicuous effects of the nonlinearity are to delay the onset of stick-slip behavior and shorten the duration of individual stick events. These effects are unsurprising, because the nonlinearity represented by the $\sinh^{-1}$ function increasingly suppresses rate weakening as the slip rate increases.

Comparison of the phase-plane diagrams shown in figures 10 and 12 demonstrates that the dynamical effects of linear and nonlinear rate weakening also differ in other ways. In both figures 10 and 12 the feature of greatest interest is the outer loop representing stick-slip limit cycles. In the limit cycles shown in both figures, the maximum positive magma pressure deviates by a factor of only 4×10^{-6} from the static equilibrium pressure (~10^7 Pa), and the maximum slip velocity is only slightly more than double the equilibrium slip velocity. The maximum velocity is somewhat larger in the case with linear rate weakening (fig. 10), however, because linear rate weakening enables a larger dynamic overshoot of slip in response to increasing magma pressure. (Here, "dynamic overshoot" means that inertia carries the moving plug upward past an equilibrium point in which forces are balanced.) This larger overshoot produces a commensurately larger decline in magma pressure in response to slip, and the magma pressure deviation at the onset of stick-slip limit cycles is about three times larger in the case with linear rate weakening than with nonlinear weakening (~6×10^{-6} versus 2×10^{-6}). This difference in pressure deviation constitutes the single most important difference between the linear case (fig. 10) and the nonlinear case (fig. 12), because the duration of stick periods (T_{stick}) increases

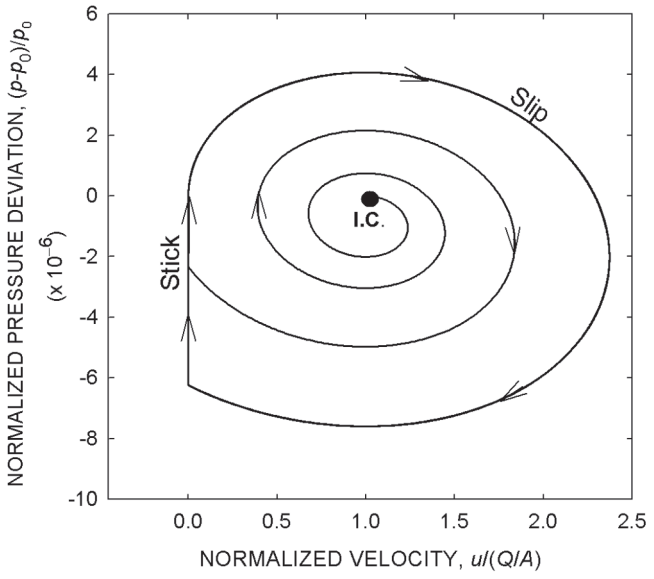

Figure 10. Phase-plane representation of simultaneous evolution of normalized slip velocity and normalized magma pressure computed for $D = -0.01$ with linear rate weakening. Initial condition (I.C.) is: $u = Q/A$, $p = p_0$, $V = V_0$. Arrows point in direction of advancing time.

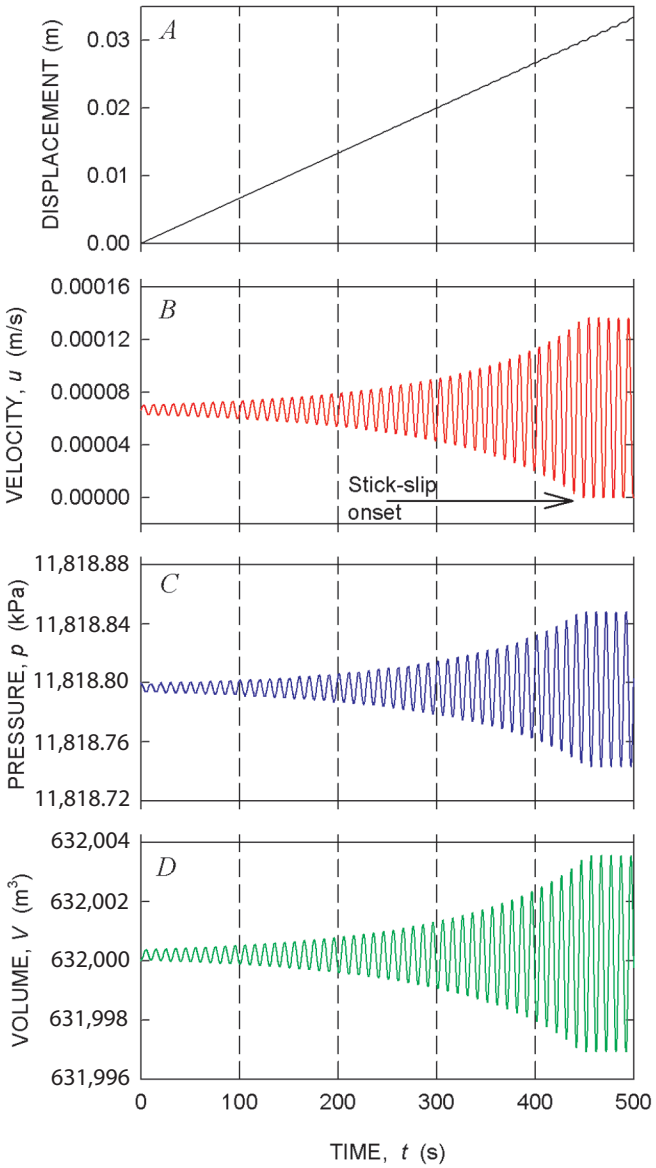

Figure 11. Start-up behavior of oscillatory solutions computed for $D = -0.01$ with nonlinear rate weakening. Initial condition is $u = Q/A$, $p = p_0$, $V = V_0$. Oscillations of slip velocity (u), magma pressure (p), and conduit volume (V) are sinusoidal until $u = 0$ occurs and stick-slip behavior begins.

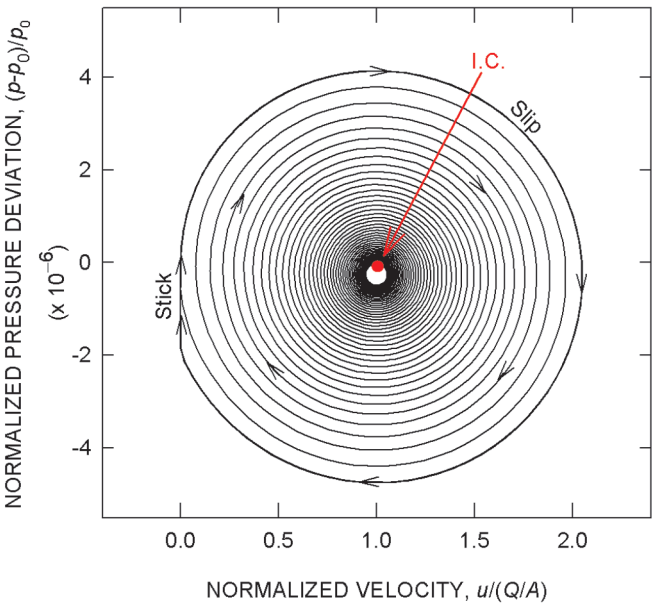

Figure 12. Phase-plane representation of simultaneous evolution of normalized slip velocity and normalized magma pressure computed for D = –0.01 with nonlinear rate weakening. Initial condition (I.C.) is $u = Q/A$, $p = p_0$, $V = V_0$. Arrows point in direction of advancing time.

exponentially with this pressure deviation, as indicated by equation 54. Therefore, nonlinearity in the friction rule has a significant effect on predictions of the periods and amplitudes of stick-slip oscillations, and the nonlinear rule was employed to generate all results presented subsequently in this paper.

Effects of the Damping Index *D*

Some of the most important findings of this study are summarized in figure 13, which illustrates computational results obtained by employing the nonlinear friction rule and various values of D. Computations that generated these results used the same parameter values used to generate figures 9–12, except that here $\lambda = 0.2$ was used, and varying values of c were used to generate D values ranging from −0.2 to −4. (The value $\lambda = 0.2$ constitutes a "best-guess" value applicable to Mount St. Helens' plug geometry and state of effective stress, and c values ranging from 1.7×10^{-5} to 3.4×10^{-4} were used to simulate subtle rate weakening similar to that observed experimentally by Moore and others, this volume, chap. 20).

Displacement time series shown in figure 13*A* were computed for a family of stick-slip cycles with various values of D, and in figure 13*B* the same results are depicted as limit cycles in the velocity-pressure phase plane. Initial conditions used to generate figure 13 assumed a static, limiting equilibrium state (u=0, $p = p_0$, $V = V_0$) rather than the state with $u = u_0$ used to generate figures 9–12. Therefore, no divergent oscillations precede the development of stick-slip limit cycles.

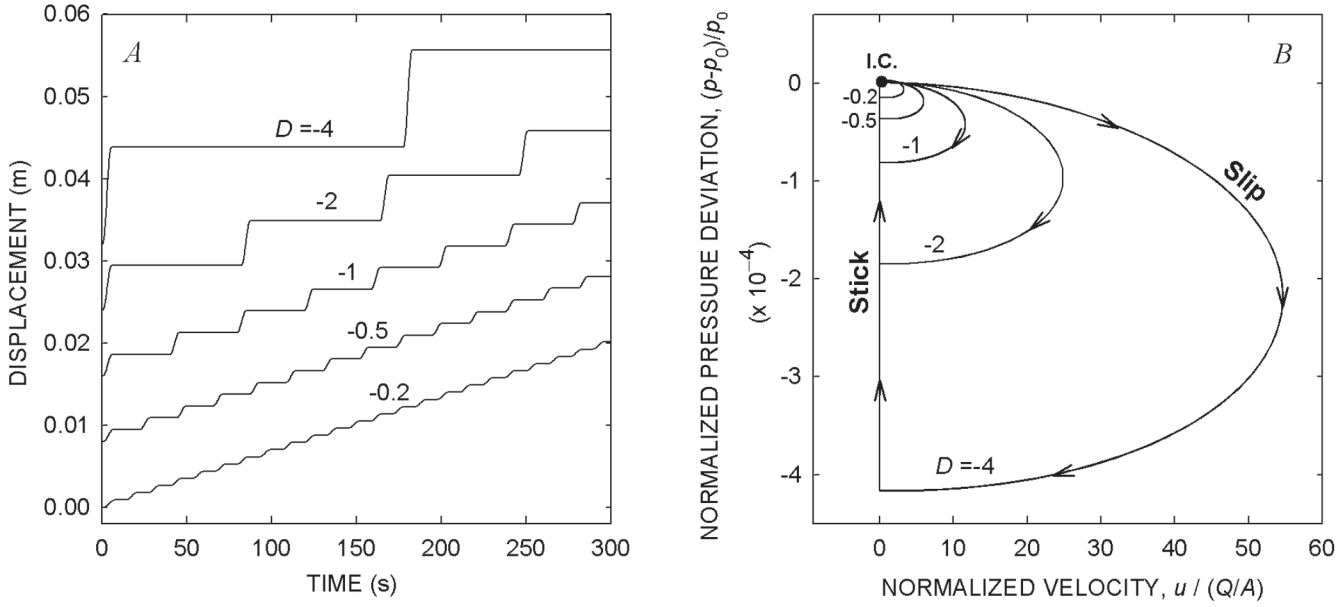

Figure 13. Stick-slip cycles computed for various values of parameter D with nonlinear rate weakening. All computations employed baseline parameter values Q=2 m^3/s, B=Q, $R_0 = 0$, K=0, Y=0, Z=0, X=5×10^{-6}, T=10 s, and employed m_0=3.6×10^{10} kg, λ=0.2, μ_0=0.5, and u_{ref}=$0.1(Q/A)$=6.667×10^{-6} m/s to determine F. Varying values of c were used to obtain varying values of D. *A*, Time series representation of stick-slip displacements. *B*, Phase-plane representation of velocity-pressure limit cycles. Arrows point in direction of advancing time.

The basic dynamics portrayed in figure 13*B* are simple. When basal magma influx produces pressure exceeding the static equilibrium value (p_0), it triggers slip at a rate that may slightly or greatly surpass the steady equilibrium rate (Q/A), depending on the value of D. When a combination of plug inertia and diminishing magma pressure no longer suffices to overcome the effects of gravity and friction, slip terminates and stick begins. Magma pressure then rebuilds until it triggers another slip event. Figure 13*A* shows that periods of stick-slip cycles with $D = -0.2$ differ little from the T=10 s period predicted by linear theory (that is, equation 25), but periods increase as D values range further from 0. For D values sufficiently far from 0, periods increase almost in direct proportion to the magnitude of D, and the amplitudes of slip events increase accordingly. Maximum slip speeds and associated pressure deviations during stick-slip cycles also increase in proportion to the magnitude of D (fig. 13*B*), bolstering the inference that D values encapsulate most of the important controls on system dynamics.

Stick-slip cycles computed with $D = -2$ closely resemble those thought to be responsible for generating drumbeat earthquakes at Mount St. Helens. With $D = -2$, individual slip events entail about 5 mm of displacement in about 5 s and maximum slip rates of ~1.7 mm/s. Attendant fluctuations in magma pressure are <0.02 percent of p_0 (fig. 13*B*), equivalent to only ~2.4 kPa or <0.2 m of static magma pressure head. This result implies that a remarkably delicate shift in the balance of forces distinguishes periods of slip from those with no slip. Multiplied by $A = 30,000$ m^2, the ~2.4 kPa pressure change also serves as a proxy for the force drop responsible for generating seismicity (~7×10^7 N).

Details of Baseline Case with D=−2

Deeper exploration of the dynamics computed with $D = -2$ provides further insight to physical phenomena that may be responsible for drumbeat seismicity at Mount St. Helens. Figure 14 illustrates details of repetitive earthquake cycles computed with D=−2. The histories of slip velocity, magma pressure, and conduit volume shown in figure 14 illustrate abrupt decreases in magma pressure and increases in conduit volume during slip events and also illustrate gradual changes of these quantities between slip events. As noted above, magma solidification at the base of the plug causes the volume of the fluid-filled conduit to decline between slip events, despite the fact that magma pressure rises.

Perhaps the most intriguing result illustrated in figure 14 involves the history of shear force along the plug margins. The shear force is large (~3.5×10^{10} N) because it must overcome the effects of both gravity and friction to move the massive plug upward, but the force drop during each slip event is comparatively small (~7×10^7 N) (fig. 14*E*). (This drop in shear force is closely related to the stress drop that occurs in conjunction with tectonic earthquakes, but force drop is, in fact, a more fundamental quantity. The force drop represents the product of the stress drop and the area of the slip surface—a product that appears directly in earthquake energy budgets (for example, Scholz, 2002, p. 184). Shear force might be concentrated in a relatively small patch of gouge bounding the extruding plug at Mount St. Helens, or it might be distributed evenly within the gouge; from the standpoint of force drop, this distinction makes no difference.) Standard estimation methods indicate that such a 7×10^7 N force drop, accompanied by 5 mm of slip (figs. 14*A*, *E*), implies about 2×10^5 J of seismic energy radiation (Scholz, 2002, p. 185), whereas the work done against friction during the slip events depicted in figure 14 is the total shear force times displacement, which yields an estimate of 2×10^8 J. These results are consistent with prior findings that only a small fraction of the work done during fault slip produces seismic radiation (McGarr, 1999).

The temporal pattern of the drop in shear force accompanying slip events also has significant implications. As slip accelerates, the shear force declines smoothly owing to the effects of rate-weakening friction (fig. 14*E*). Similarly, as slip decelerates, the force smoothly rises as friction gradually increases. When slip stops, however, the shear force drops abruptly because it suddenly returns to a static equilibrium value imposed by the plug weight and magma-pressure force, which has declined during slip. Before this reequilibration, the shear force is out of equilibrium with these static forces because rate-weakening friction allows slip to dynamically overshoot the equilibrium point. The net effect is that almost the full force drop (~7×10^7 N) occurs abruptly at the end of the slip cycle, and it thereby provides an impulse capable of radiating high-frequency seismic energy.

Sensitivity of Behavior to Variations of Parameters Within D

Values of D encapsulate the effects of most of the important parameters affecting stick-slip dynamics, but it is nevertheless necessary to examine whether variations in values of these individual parameters have significant effects. Results presented in figures 15 and 16 show that the behavior computed for D= −2 is quite insensitive to variations in c, λ, and u_0 / u_{ref}. For example, if values of c and λ range over orders of magnitude, while D is held constant, computed stick-slip limit cycles differ only slightly in a phase-plane diagram depicting coevolution of the normalized pressure deviation and normalized slip velocity (fig. 15*A*). Differences exist exclusively in the magnitude of normalized pressure deviations, reflecting the fact that smaller λ values imply that less magma pressure is needed to satisfy limiting equilibrium and trigger slip. Moreover, if the pressure deviations are "denormalized," as shown in figure 15*B*, such differences disappear entirely, and results for all values of c and λ collapse onto a single curve in the phase plane. This finding demonstrates that values of c and λ individually are unimportant in the system's dynamical behavior, provided that D is constant and the nonlinearity of the friction rule is unchanged.

Results shown in figure 16 illustrate the effects of changing the nonlinearity of the friction rule by allowing

the value of u_0 / u_{ref} to range over four orders of magnitude while holding D= −2. To facilitate comparison with figure 13, figure 16 depicts results as both displacement time series and stick-slip limit cycles. These results show that reducing values of u_{ref} (that is, increasing values of u_0 / u_{ref}) produces stick-slip cycles with increased interevent periods, increased slip displacements, increased slip velocities, and increased deviations of magma pressure from its equilibrium value. However, effects of u_0 / u_{ref} ranging over four orders of magnitude (fig. 16) are similar to the effects of D ranging from about −2 to −4 (fig. 13), reinforcing the view that D values encapsulate most of the dynamical controls on system behavior. It is, however, unsurprising that effects of u_0 / u_{ref} are not captured entirely by values of D, as the effect of u_0 / u_{ref} is inherently nonlinear. For values of u_0 / u_{ref} smaller than 1, the periods of stick-slip oscillations lengthen, but this behavior is not pursued here because it has little relevance to plug extrusion at Mount St. Helens.

Effects of Plug Mass Change (Nonzero *K*)

Continuous changes in plug mass are represented by nonzero values of K (and of κ, its dimensional equivalent). If the condition B=Q is assumed, nonzero values of K imply that the rate of mass loss due to surface erosion ($\rho_r E$) does not balance the rate of mass gain due to basal accretion (ρB), and the simplest example of such an imbalance occurs when the erosion rate is zero and the plug mass increases at the rate $\kappa = \rho B$. Figure 17 illustrates time-series behavior computed for this case (that is, κ=4,000 kg/s; K=1.78×10^{-7}) with D= −2 and $u_0 / u_{ref} = 10$. Comparison of figure 17 with figure 14

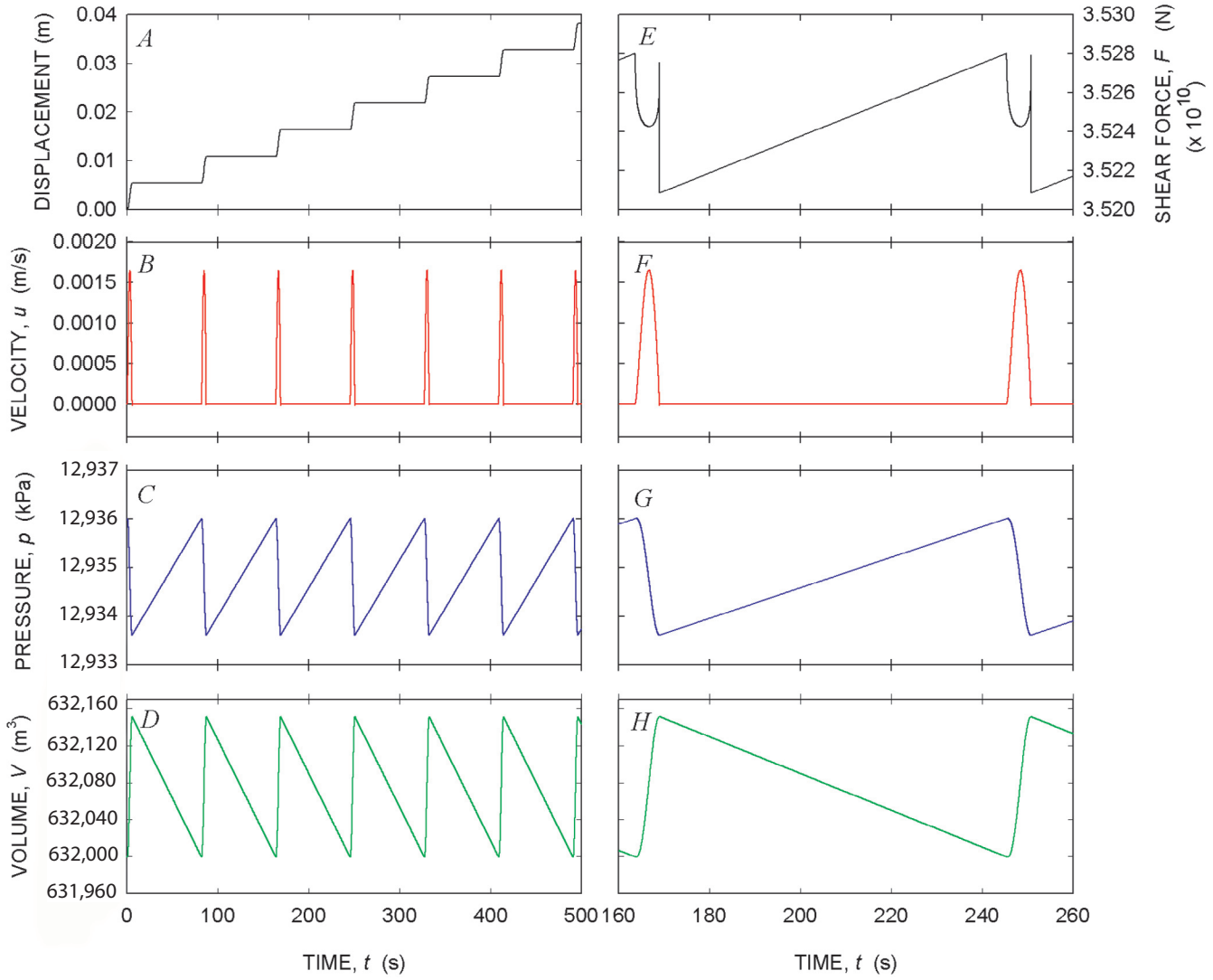

Figure 14. Time series depiction of concurrent changes in plug displacement, slip velocity, magma pressure, and conduit volume during earthquake cycles computed for baseline case with D = −2. Parameter values are same as those used to generate figure 13, and c = −1.71×10^{-4} is used to obtain D = −2. Panels *A*–*D* illustrate behavior during seven consecutive slip events, and panels *E*–*H* show details on an expanded time scale. Panel *E* is distinct from other panels because it shows force drops accompanying slip events.

shows that stick-slip cycles computed with $K>0$ have slightly larger periods and amplitudes than those computed with $K=0$, an unsurprising finding in view of analytical results indicating that positive K values will cause growth of oscillation periods (see equation 33). However, in contrast to analytical predictions, periods and amplitudes of stick-slip cycles computed with $K>0$ do not change with time.

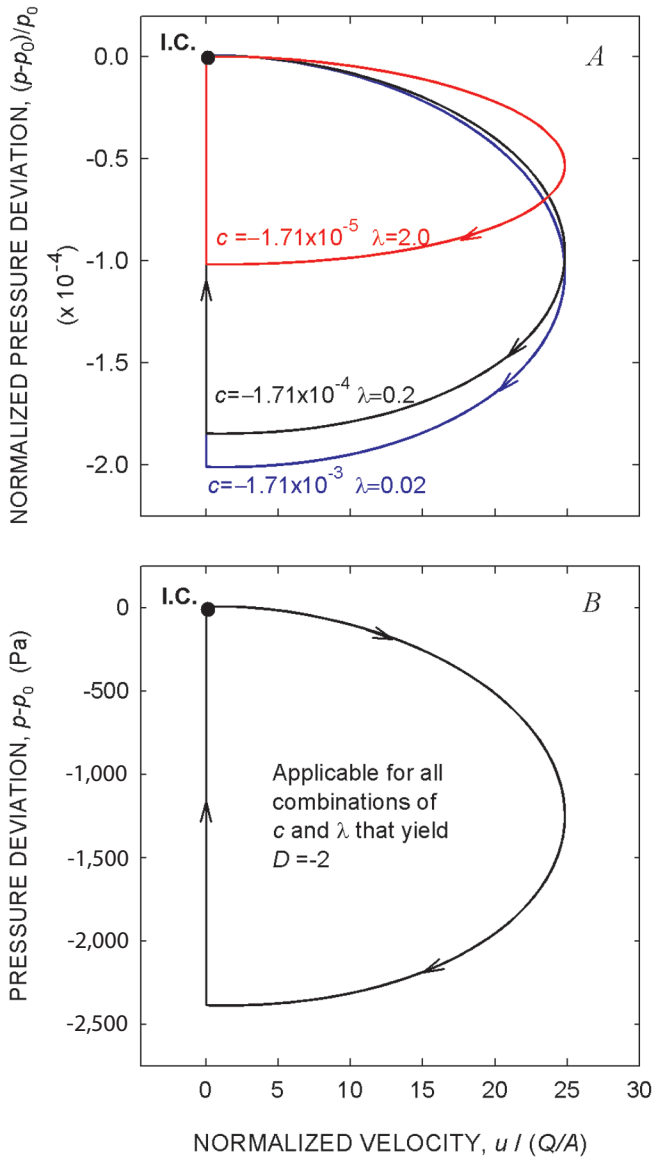

Figure 15. Sensitivity of stick-slip behavior with $D = -2$ to variations in parameters c and λ in the nonlinear rate-weakening friction rule. Other parameter values are same as those used to generate figure 14. Only phase-plane representations are shown, because time series are identical in all cases. Arrows point in direction of advancing time. *A*, Stick-slip cycles represented in terms of normalized pressure deviations. *B*, The same stick-slip cycles represented in terms of physical pressure deviations.

The linear analytical model yields spurious predictions of the effects of positive K values because it neglects explicit coupling between magma-pressure change and conduit-volume change, which is included in the nonlinear computational model. Figure 17 shows that magma pressure rises slightly in each successive stick-slip cycle, because increased pressure is required to drive uplift of the increasingly massive plug. This increasing pressure is accompanied by slightly decreasing conduit volume (fig. 17), because volume change due to compression of the highly compliant magma exceeds volume change due to conduit-wall deflection. Moreover, the percent decrease in conduit volume at the end of each stick-slip cycle is precisely the same as the percent increase in plug mass during the same cycle. Therefore, the effects of changes in conduit volume counterbalance the effects of changes in plug mass, such that the net effect of these changes on the oscillation period is zero. (As shown by equation 25, the time scale for the natural oscillation period, t_0, depends on the product of plug mass and conduit volume.) Numerical results show that the counterbalancing effect of mass changes and volume changes occurs for all positive K values—within reason. As suggested by analytical results, however, very large K or κ values (satisfying the criterion $\kappa > -(2/3)C$) might stabilize extrusion and diminish oscillations. Such large κ values are physically unreasonable, because C scales with the large quantity $m_0 g / u_{ref}$ (equation 23*B*), and mass accretion at a commensurately large rate is not plausible.

The magma pressure build-up depicted in figure 17 is further illustrated by its phase-plane representation in figure 18. As shown in the phase plane, each stick-slip limit cycle is like the preceding cycle, except that each successive slip event begins at a successively larger magma pressure. In this example, use of the maximum plausible rate of mass increase (that is, $\kappa = \rho B = 4{,}000$ kg/s) causes magma pressure to double after about 115,000 stick-slip cycles, or about 113 days. To within 1 percent, this result agrees with the pressure doubling time calculated by applying the analytical formula derived for pseudosteady-state extrusion (that is, equation 21) for the case in which $\kappa = 4{,}000$ kg/s. The chief implication of these results is that if the plug mass increases significantly, magma pressure can increase significantly without increasing the extrusion rate. Conversely, changes in extrusion rate need not be linked to changes in magma pressure if the plug mass changes.

Computational results obtained with $K<0$ differ in important ways from results obtained with $K>0$. Figure 19 depicts results computed using a negative K value with the same magnitude as the positive K value used to generate figures 17 and 18 (that is, $K = -1.78\times10^{-7}$), and this value implies that the mass erosion rate, $\rho_r E$, is twice the rate of basal mass accretion, ρB. Comparison of figures 17 and 19 shows that the negative K value produces changes in magma pressure and conduit volume with signs opposite to those for $K>0$ and also produces more frequent slip events (seven as opposed to six in 500 s). Slip events occur more frequently in the presence of diminishing plug mass, because less magma

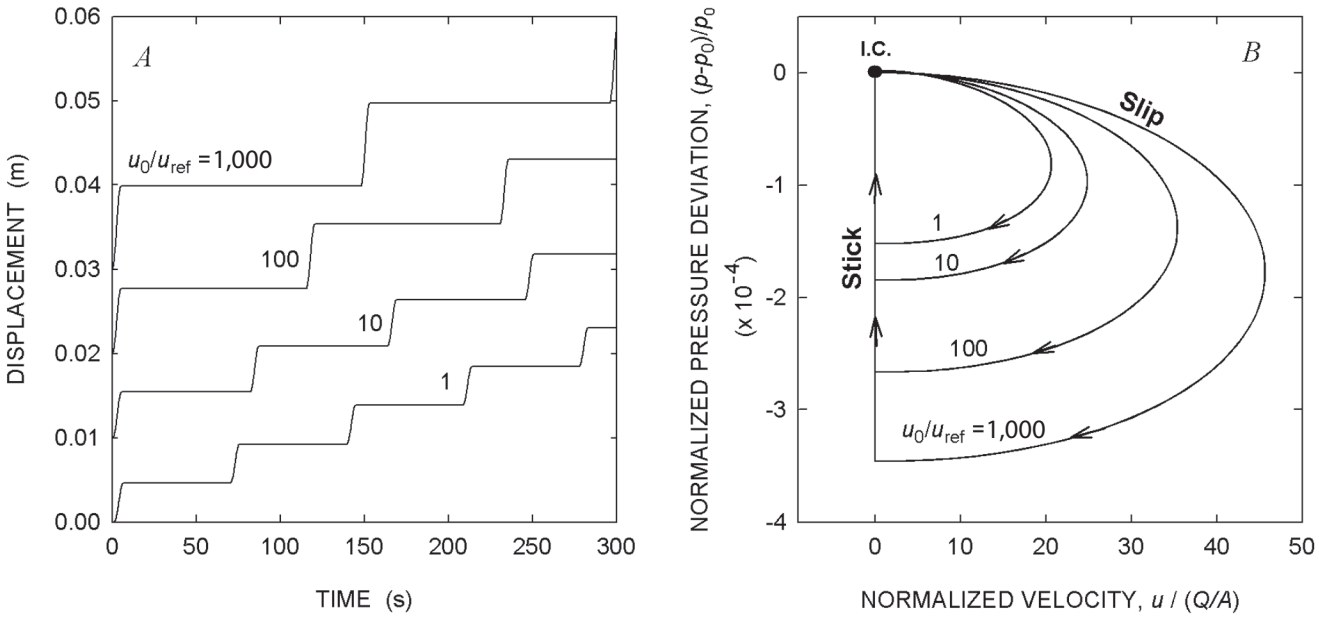

Figure 16. Sensitivity of stick-slip behavior with D = –2 to variations in u_0 / u_{ref} in the nonlinear rate-weakening friction rule. Other parameter values are the same as those used to generate figure 14. *A*, Time-series representation of stick-slip displacements. *B*, Phase-plane representation of velocity-pressure limit cycles corresponding to *A*. Arrows point in direction of advancing time.

pressure is necessary to trigger slip in each successive stick-slip cycle. Importantly, the increased frequency of slip events is accompanied by an increase in the mean extrusion rate (which occurs with a constant magma supply rate, Q=2 m^3/s), and this increase demonstrates the potential for runaway eruptive behavior. Moreover, decreasing plug mass eventually leads to a singularity in which fluid magma reaches the surface and the SPASM equations no longer apply (that is, the case with C<0 and κ<0 identified in table 3).

Runaway behavior is more evident in computational results obtained using negative K values with magnitudes much larger than the value -1.78×10^{-7} used to generate figure 19. Unlike large positive K values, large negative K values are physically plausible, because the plug mass can decrease rapidly if large-scale spalling or avalanching erodes the plug surface. Figure 20 depicts displacement time series computed with negative K values having magnitudes 100, 1,000, and 10,000 times greater than -1.78×10^{-7}. (The value -1.78×10^{-3} corresponds to mass loss at a rate of 4×10^7 kg/s or a volumetric rate of about 20,000 m^3/s—a rate high enough to remove the entire plug in less than one hour.) The key point illustrated by figure 20 is that, in the presence of significant mass loss, time-averaged displacement rates can be much larger than the steady equilibrium rate $u_0 = Q / A = 6.667\times10^{-5}$ m/s that prevails with K=0, and these high rates would likely lead to a change in eruptive style.

The unstable growth of extrusion rate that occurs with K= -1.78×10^{-3} is represented in the phase-plane diagram depicted in figure 21. The diagram shows that deviations from the equilibrium magma pressure and equilibrium slip rate are exceedingly large during each stick-slip cycle and that maximum slip rates increase during each successive slip cycle—while magma pressure successively declines. In such scenarios, then, extrusion occurs faster and faster until the plug is removed and liquid magma reaches the surface. The accompanying decline in magma pressure could also result in increased vesiculation and explosive potential, although this process is not represented by the SPASM model.

Effects of X

The dimensionless parameter X defined in equation 44 mediates the interaction between extrusion rate and conduit volume change, as shown by equations 42 and 48, and it also affects magma pressure change through its influence on R^* (that is, equation 45). The physical meaning of X can be clarified by writing its definition in a simplified, approximate form that is valid if $\alpha_1 >> \alpha_2$, which is almost certainly the case at Mount St. Helens:

$$X \approx u_0 \left(\frac{\alpha_1 m_0}{V_0} \right)^{1/2}. \qquad (55)$$

This definition implies that, for systems in which u_0 and α_1 are constant, variations in X can be viewed as scaled variations in m_0 / V_0. Indeed, because values of m_0 / V_0 can be changed while holding t_0 and D constant, this strategy is used

to assess the effects of variations in X computationally. The condition K=0 is also assumed in this assessment.

Computations in which X is increased or decreased by one order of magnitude from its baseline value (5×10^{-6}) show that stick-slip time series and phase-plane diagrams are identical for all values of X. However, figure 22 shows that some important details of the earthquake cycle change when X is increased by an order of magnitude (to 5×10^{-5}) by simultaneously increasing m_0 and decreasing V_0 by one order of magnitude each from their baseline values, while retaining D= −2. Comparison of figure 22 with figure 14 (the baseline case) shows that, although the timing and magnitude of slip events is unchanged when X is increased by one order of magnitude, the accompanying magma pressure, pressure change, shear force, and force drop are each increased by one order of magnitude, whereas the conduit volume change is reduced by somewhat less than an order of magnitude. These effects are all logical consequences of the increased plug mass and reduced conduit volume that are imposed by increasing the value of X.

The most important fact illustrated by figure 22 is that the predicted magma pressure at the base of the plug (~1.3×10^{8} Pa) is roughly an order of magnitude larger than the expected lithostatic pressure near the plug base (that is, at depths ~500 m). Such a large magma pressure is unrealistic, as it would probably cause hydraulic fracturing and a marked change in eruption style. This result implies that a value $X\approx5\times10^{-5}$ is too large to be realistic. Similarly, if X is reduced to 5×10^{-7} while holding t_0 and D constant, computed basal magma pressures are an order of magnitude smaller than the likely lithostatic pressure—a result that is also unrealistic. These findings imply that an X value similar to the baseline value (5×10^{-6}) is probably appropriate for Mount St. Helens. Therefore, the computed drop in shear force accompanying slip in the baseline case (fig. 14) is also probably appropriate.

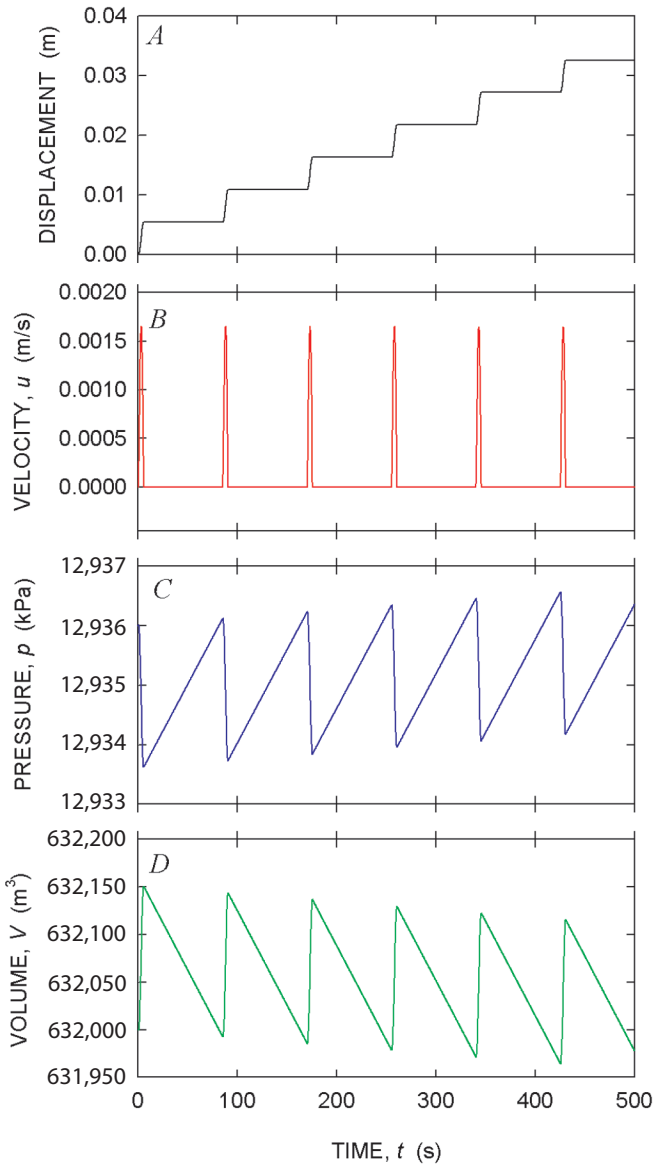

Figure 17. Time-series behavior of solutions computed with D= −2, u_0/u_{ref}=10, and increasing plug mass specified by K=1.78×10^{-7} (that is, κ =4,000 kg/s). Other parameter values are same as those used to generate figure 14.

Effects of Y

The dimensionless parameter Y defined in equation 44 represents the scaled difference between the magma-

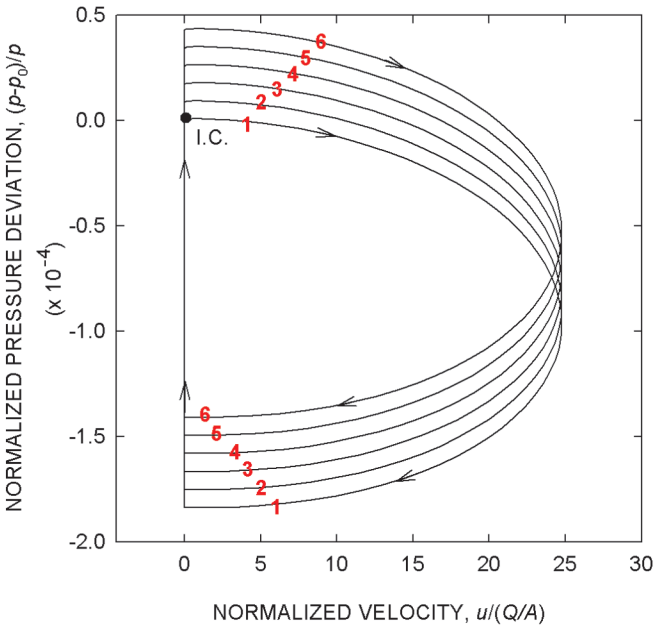

Figure 18. Phase-plane representation of solution depicted in figure 17. Numbers shown in red denote time sequence of successive limit cycles. Arrows point in direction of advancing time.

influx rate Q and magma-solidification rate B. All results presented thus far assume that $B=Q$, which is necessary for the magma-plug system to long remain close to equilibrium. Indeed, if $B \neq Q$ for a sustained period, a transition in eruptive behavior is inevitable. If $B>Q$, for example, the solidification front would propagate downward and the plug mass would increase unless mass loss due to surface erosion balances mass gain due to basal accretion. If such a balance were sustained, the plug would appear to sink progressively, even as extrusion continued, and friction on the plug margins would progressively increase. On the other hand, if $B<Q$, the solidification front would migrate

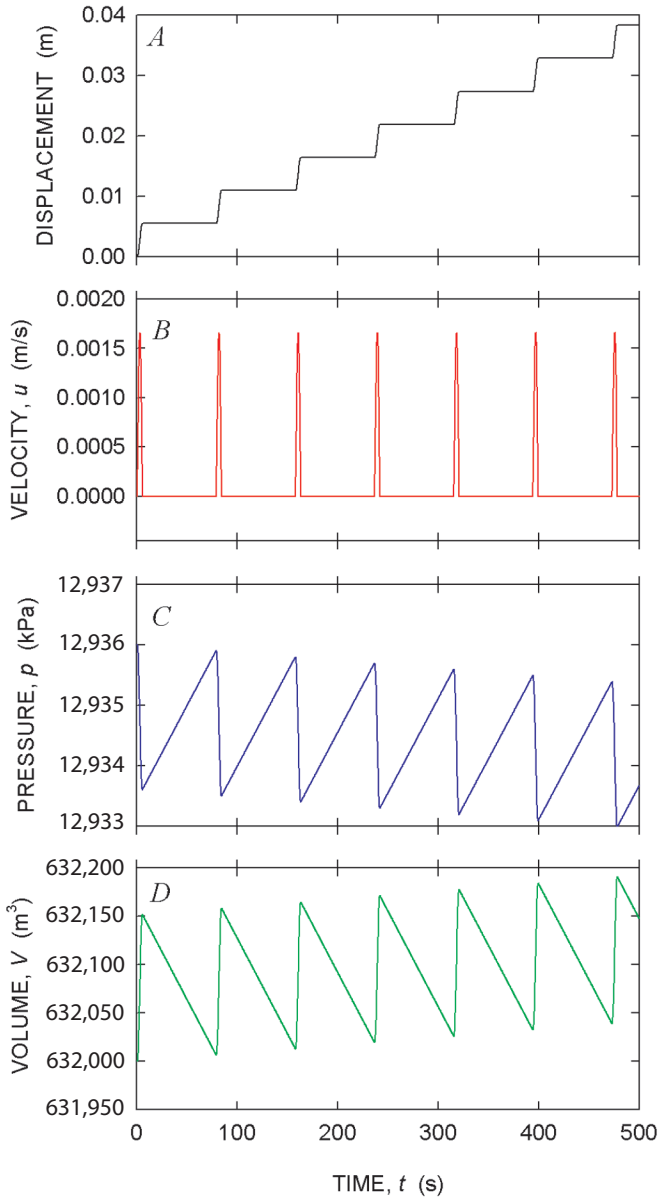

Figure 19. Time-series behavior of solutions computed with $D=-2$, $u_0/u_{ref}=10$, and decreasing plug mass specified by $K=-1.78\times10^{-7}$ (that is, $\kappa=-4{,}000$ kg/s). Other parameter values are same as those used to generate figure 14.

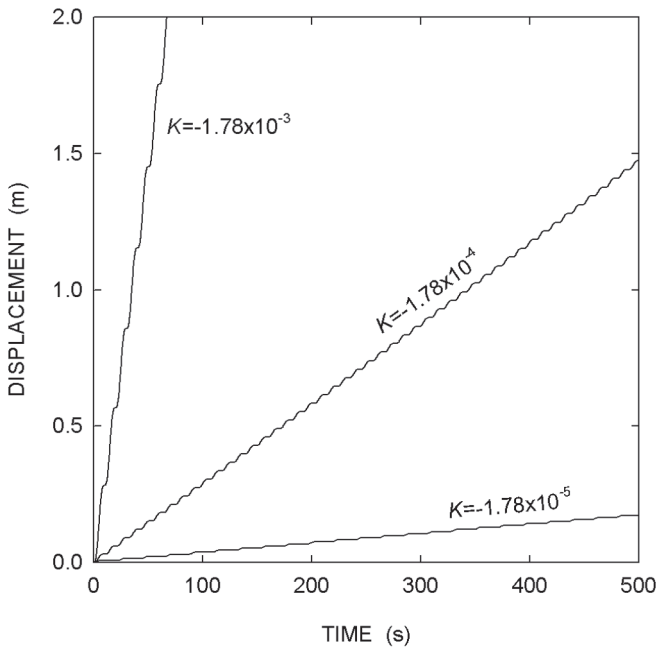

Figure 20. Comparison of displacement time series computed with $D=-2$, $u_0/u_{ref}=10$, and differing rates of decreasing plug mass specified by differing values of K. Other parameter values are same as those used to generate figure 14.

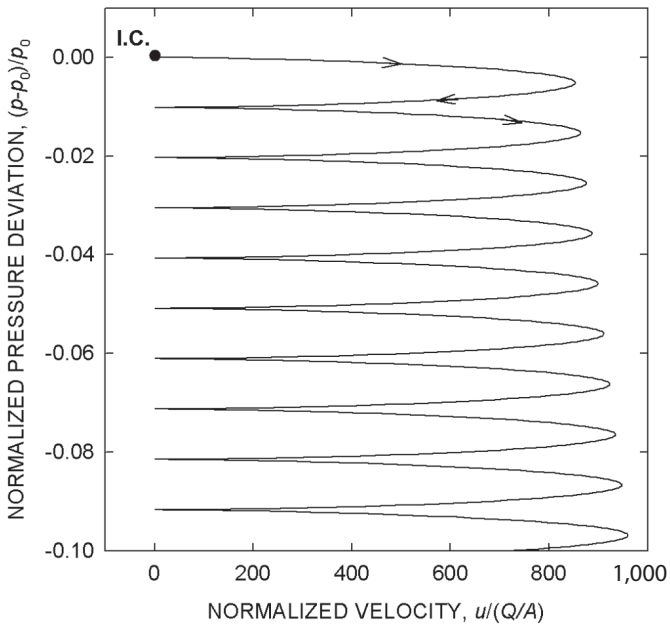

Figure 21. Phase-plane representation of stick-slip limit cycles occurring with $D=-2$, $u_0/u_{ref}=10$, and rapid decrease in plug mass ($K=-1.78\times10^{-3}$; $\kappa=-4\times10^{7}$ kg/s). Other parameter values are same as those used to generate figure 14. Arrows point in direction of advancing time.

upward. In the extreme case of B=0, any changes in plug mass would result exclusively from surface erosion, and the plug would eventually be pushed out the ground as liquid magma reached the surface. This scenario represents singular behavior analogous to that occurring with a negative mass-change rate (K<0). Below, I focus only on short-time behavior for cases with $B>Q$ and B=0.

Behavior computed for a case with B=2Q=4 m^3/s and K=1.78×10^{-7} (that is, κ=4,000 kg/s) is shown in figure 23; this case is exactly like that illustrated in figure 17 except that, here, growth of plug mass occurs as a result of basal accretion in excess of Q. Thus, figure 23 depicts the response to growth of mass exclusively below the surface (with downward migration of the solidification front), whereas figure 17 depicts the response to growth exclusively above the surface (with no downward migration of the solidification front). The results shown in figures 23 and 17 are in most respects identical, except that the conduit volume decreases much more quickly in the case with basal accretion in excess of Q (fig. 23)—an obvious consequence of downward migration of the solidification front. Increasing pressurization of the conduit fluid accompanies this migration, and in the long run this combination of effects is unsustainable because magma pressure eventually would become large enough to fracture surrounding rock.

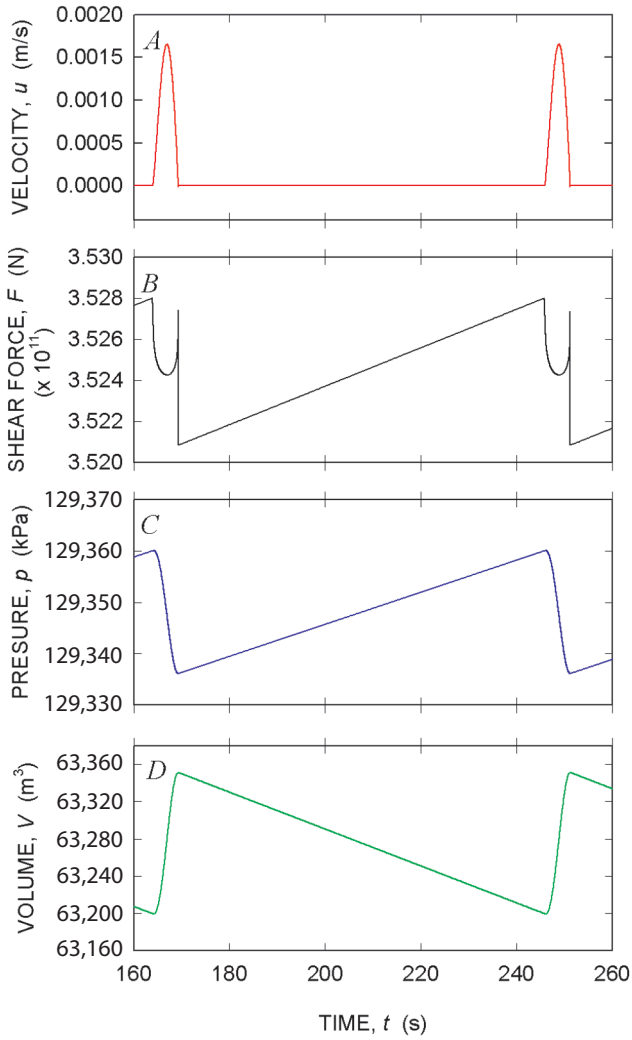

Figure 22. Details of an earthquake cycle computed with D = –2, u_0/u_{ref}=10, and X = 5×10^{-5} (one order of magnitude larger than the X value used to compute the baseline results shown in figure 14). Other parameter values are same as those used to generate figure 14.

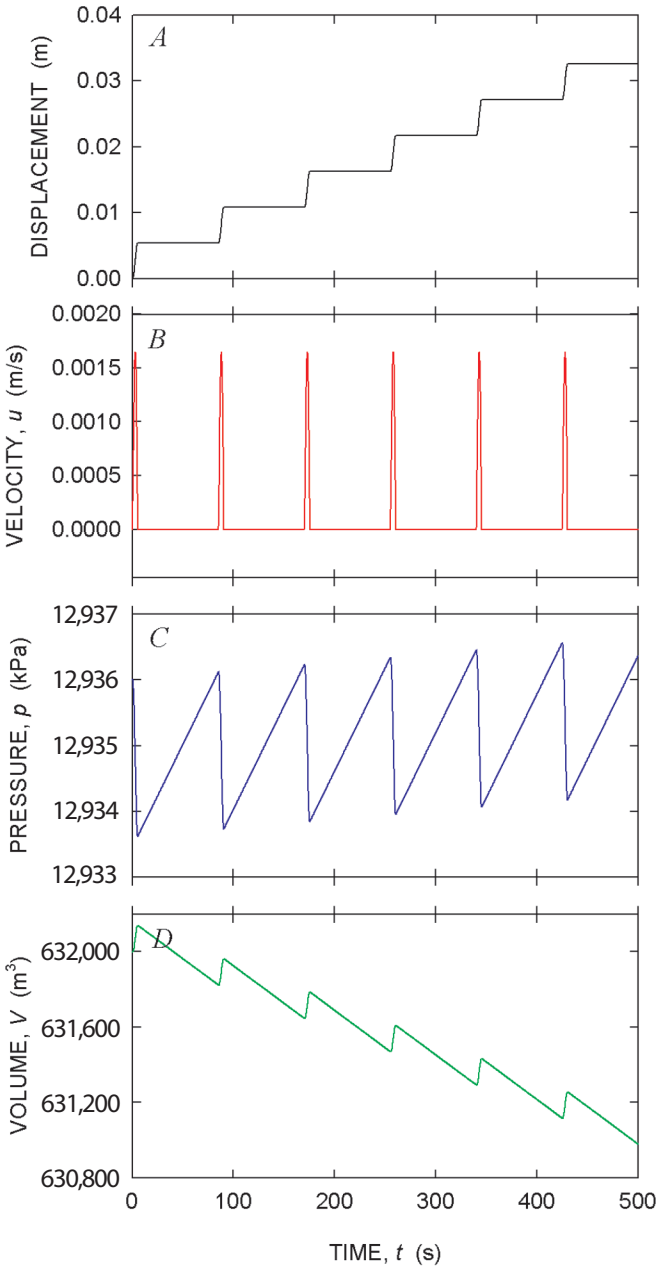

Figure 23. Time series behavior of solution computed with D = –2, u_0/u_{ref}=10, and excess basal accretion specified by B = 2Q = 4 m^3/s and K = 1.78×10^{-7} (that is, κ = 4,000 kg/s). Here Y = –5×10^{-6}. Other parameter values are same as those used to generate figure 14.

The limiting case with small B (that is, B=0) exhibits behavior almost exactly like that computed for the baseline case with B=Q and K=0. Indeed, with B=0, graphs of the behavior for early times are indistinguishable from those shown in figures 13 and 14, except that conduit volume increases with each successive stick-slip cycle (fig. 24). This increase is an obvious consequence of upward migration of the base of the plug, and although this migration affects plug dynamics negligibly in the short term, persistence of this migration eventually must lead to the singularity noted above (that is, magma reaching the surface).

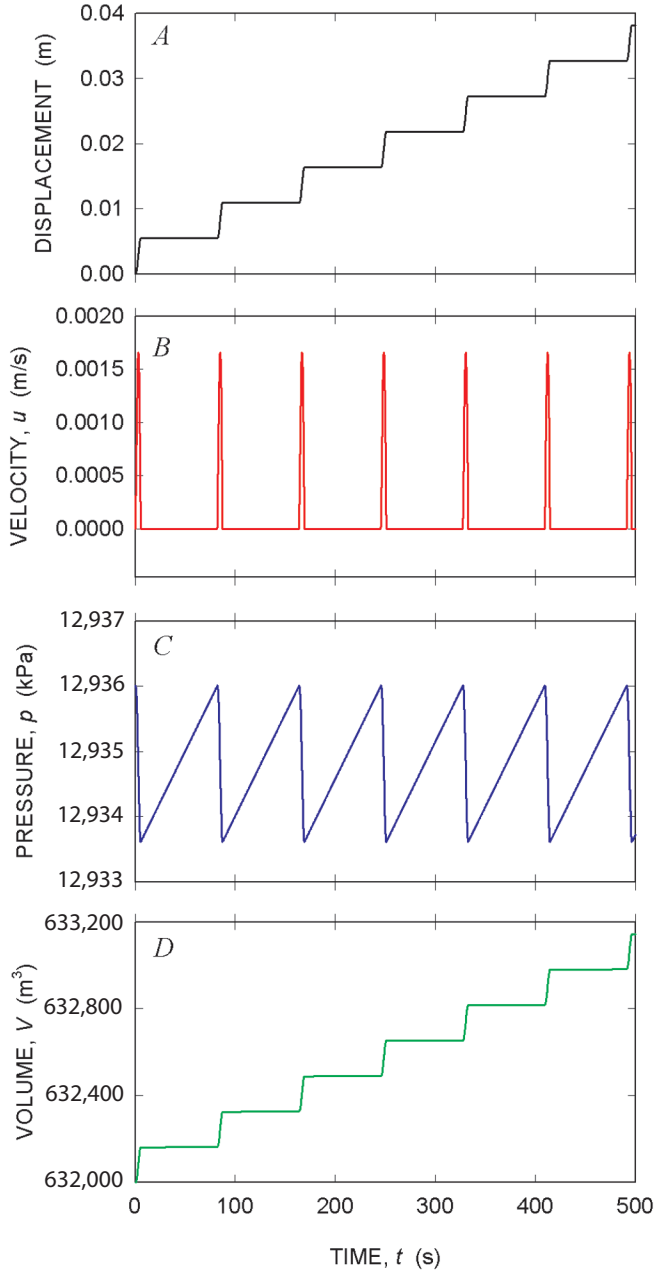

Figure 24. Time series behavior of solution computed with D = –2, u_0/u_{ref}=10, and zero basal accretion (B = 0). Here Y = 5×10^{-6}. Other parameter values are same as those used to generate figure 14.

Effects of Z

The dimensionless parameter Z defined in equation 44 may be interpreted as a scaled version of the mass-density ratio difference, $R_0 = 1-(\rho_0/\rho_r)$, which plays its most important role in determining the mean (that is, time-averaged) extrusion rate, $u_0 = (Q - R_0 B)/A$ given by equation 19. The mean extrusion rate is affected by Z because R_0 determines the change in density that occurs as magma ascending at rate Q solidifies at rate B—such that an increase in density during solidification reduces the volumetric extrusion rate of the solid plug. Values of R_0 plausibly range from about −0.5 to 0.5, and for the case with B=Q, these values yield u_0 values ranging from 0.5(Q/A) to 1.5(Q/A). Moreover, with B=Q, the definition of Z also reduces to $Z = R_0/(1-R_0)$, so that Z depends exclusively on R_0. Examples of displacement time-series solutions computed for this case, with various values of Z, are shown in figure 25.

Interpretation of figure 25 is complicated by the fact that with A and B held constant, values of Z cannot be varied independently of values of D and X (because Z, X, and D all depend on u_0, which in turn depends on R_0). Therefore, the figure shows results of computations in which Z, X, and D vary simultaneously. Nevertheless, the effect of values of Z on the average extrusion rate is clearly evident in figure 25; large departures from the baseline value Z=0 yield similarly large departures from the average extrusion rate observed with Z=0 (that is, $u_0 = Q/A$). The period of stick-slip cycles remains nearly proportional to the magnitude of D (just as in the baseline case illustrated in fig. 13), despite variations in Z. Unlike

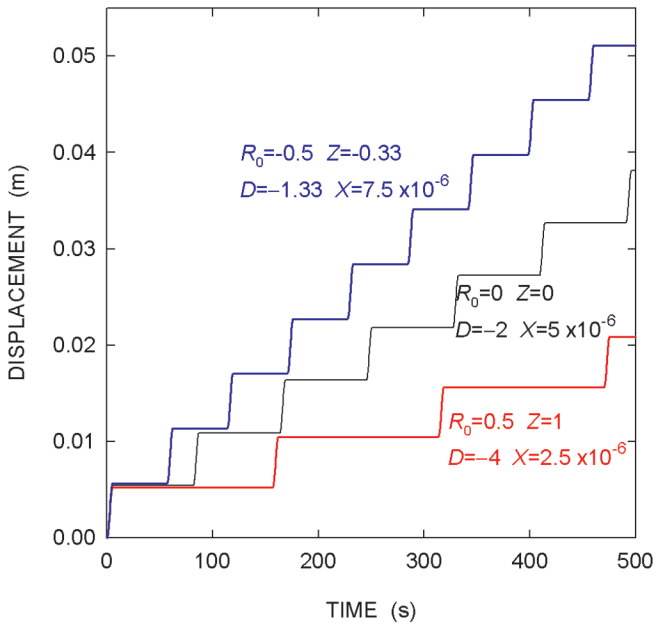

Figure 25. Displacement time series computed with varying values of R_0 and Z (with accompanying variation of D and X). Other parameter values are same as those used to generate figure 14.

the baseline case, however, the time series depicted in figure 25 each involve slip events with about the same magnitude of displacement (~5 mm). This behavior indicates that, while D largely controls the system's dynamics, the magnitude of slip events is additionally regulated by Z.

Effects of Initial Conditions

The preceding results were computed using initial conditions that assume a state of mechanical equilibrium, but volcanic eruptions presumably begin with an initial disequilibrium state, such as that due to magma pressure in excess of the static limiting equilibrium pressure ($p > p_0$). This section summarizes results of computations that used a disequilibrium initial condition of this type.

All computations with $p > p_0$ predict that an initial pulse of rapid motion occurs until plug momentum is depleted, magma pressure relaxes, and static equilibrium is restored, and this behavior occurs irrespective of the sign or value of D (figs. 26, 27). Pressure then rebuilds until it triggers a second stage of motion. For $D<0$ this stage consists of endlessly repetitive stick-slip limit cycles (closed loops in fig. 26) exactly like those produced with equilibrium initial conditions (for example, fig. 13), whereas for $D>0$ the second stage converges to a fixed-point equilibrium representing a state with dynamically balanced forces (fig. 27). It is noteworthy, however, that cases with rate-strengthening friction ($D>0$) and rate-weakening friction ($D<0$) exhibit similar initial pulses if the initial pressure disequilibrium is the same (for example, compare results for $D=\pm 0.2$ in figs. 26*A* and 27).

A key point illustrated in figure 26 is that the maximum speed of the initial extrusion pulse and the magnitude of the associated pressure deviation increase almost linearly with increasing initial magma overpressure. Moreover, this trend is insensitive to the value of D, and linear extrapolation can therefore be used to infer the maximum extrusion speed (and pressure deviation) associated with any initial overpressure. With $D= -2$, for example, each increase of 0.005 percent in initial overpressure increases the maximum speed of the initial movement pulse u_{max} by about $u_{max}/(Q/A) = 14$ (fig. 26*B*).

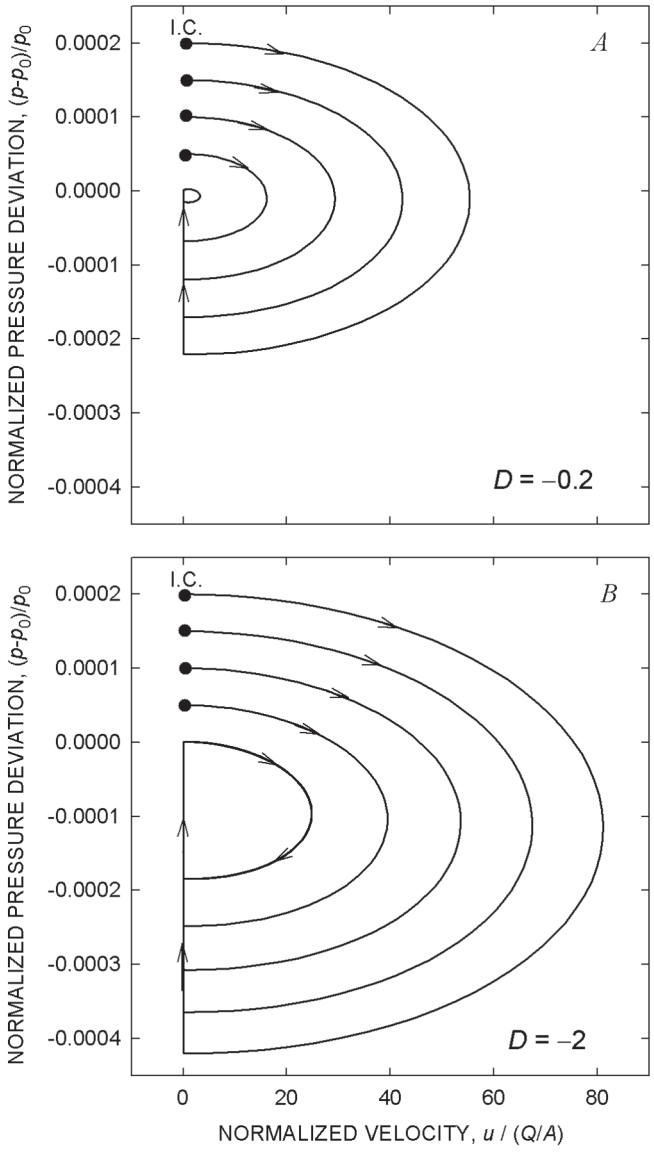

Figure 26. Phase-plane representation of behavior computed with four disequilibrium initial conditions (that is, initial excess magma pressures 0.005 percent, 0.01 percent, 0.015 percent, and 0.02 percent of p_0), for each of two negative values of D. Parameter values are same as those used to generate figure 14, except that $c = -1.71\times10^{-5}$ is used to obtain $D = -0.2$. Arrows point in direction of advancing time. *A*, $D = -0.2$. *B*, $D = -2$.

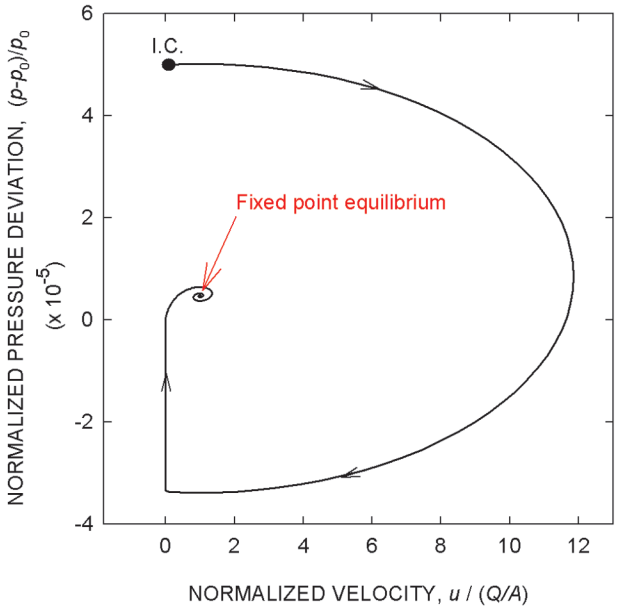

Figure 27. Phase-plane representation of extrusion behavior computed with an initial excess magma pressure (0.005 percent of p_0) and $D = 0.2$. Parameter values are same as those used to generate figure 14, except that $c = 1.71\times10^{-5}$ is used to obtain $D = 0.2$. Arrows point in direction of advancing time.

In conjunction with the baseline value Q/A=6.67×10^{-5} m/s for Mount St. Helens, this result implies that a 0.005 percent magma overpressure (relative to the static limiting equilibrium pressure p_0) would produce a maximum extrusion velocity of about 3 mm/s, and that an overpressure of 5 percent would produce a maximum extrusion velocity of ~1 m/s.

Magnitudes of displacements that occur during the initial movement pulses shown in figures 26 and 27 can be estimated from the maximum pressure deviation $p_0 - p$, because the displacement during slip is proportional to the duration of the subsequent "stick time" (as shown by equation 54). By inference from equation 54, then, the displacement during the initial slip event increases like $e^{(\alpha_1+\alpha_2)(p_0-p_i)}$. On this basis, extrapolation from figure 26*B* shows that initial magma overpressures of even a few percent would lead to movement pulses of at least several meters, provided that D= −2.

Discussion

The SPASM model was developed to explain the relation between nearly steady solid-state extrusion and nearly periodic drumbeat earthquakes observed during the 2004–5 eruption of Mount St. Helens. Although this relation could result from a complicated interaction of numerous physical and chemical processes, the SPASM model aims for a parsimonious mechanical explanation that employs a minimum of postulates and variables. Some of the parsimony of the SPASM model derives from its central, simplifying assumption: that the volumetric flux of magma into the base of the eruption conduit (Q) is constant. This assumption is consistent with a top-down perspective of eruption dynamics, in which no time-dependent changes in a deep magmatic system are invoked to explain phenomena observed at Earth's surface.

From a mathematical standpoint, the assumption of constant Q enables the SPASM model to be reduced to a nonlinear system of three first-order ordinary differential equations. The relative simplicity of these equations facilitates both analytical and numerical studies of model properties. Indeed, the mathematical behavior of the SPASM model can be understood completely, and understanding of this simple model provides a steppingstone toward understanding behavior of Mount St. Helens during solid-state extrusion in 2004–5.

Analytical study of the SPASM model demonstrates that steady, solid-state extrusion is an equilibrium condition that can be satisfied exactly if the magma influx rate, Q, equals the rate of magma solidification at the base of an extruding plug, B, which in turn is balanced by erosion of the plug surface, E. In addition, pseudosteady states can exist in which the extrusion rate remains constant and changes in plug mass are accompanied by compensating changes in magma pressure. Such pseudosteady states cannot persist indefinitely, however, because changes in plug mass and magma pressure cannot continue without eventually causing a change in eruption style. Therefore, long-term steady-state extrusion at Mount St. Helens in 2004–5 probably involved a near-equilibrium state in which the plug mass effectively remained almost constant and $B \approx Q$ applied.

Analysis of the SPASM model shows that, even when a near-steady eruptive state persists, extrusion velocities have an inherent tendency to exhibit short-term oscillations about the long-term equilibrium rate. These oscillations are an inevitable consequence of the interaction of plug momentum, a variable upward force due to magma compression and pressure, and a downward force due to the plug weight. The oscillations are damped mostly by plug-boundary friction, and if friction exhibits rate-weakening behavior like that observed in experiments with fault gouge obtained from the surface of the Mount St. Helens plug, damping is negative and oscillation amplitudes grow unstably. Oscillation growth is necessarily arrested, however, because friction has the potential to reverse its direction of action when the plug extrusion velocity declines to zero. Growing oscillations are thereby transformed to repetitive stick-slip cycles, and these cycles continue indefinitely (that is, until a change in a parameter such as Q, B, or E occurs). According to the SPASM model, these repetitive stick-slip cycles are responsible for generating nearly periodic "drumbeat" earthquakes observed during solid-state extrusion at Mount St. Helens in 2004–5.

Properties of stick-slip cycles predicted by the SPASM model are controlled by a variety of factors, but both analytical and numerical results support the conclusion that the natural oscillation time scale t_0 and dimensionless damping D exert the most important controls. The oscillation time scale is fixed by conduit and plug properties that affect elastic strain in the system, whereas nonlinearly rate-dependent friction causes damping to vary as a function of the extrusion velocity u. Nevertheless, computational results show that most effects of variable damping are encapsulated by D evaluated at the steady equilibrium extrusion rate, $u = u_0$. These results show that the amplitudes and periods of stick-slip cycles increase almost in proportion to the magnitude of D, provided that t_0 remains constant.

Computations using diverse values of D show that D= −2 produces stick-slip cycles most similar to those inferred to generate drumbeat earthquakes at Mount St. Helens throughout much of the 2004–5 eruption, and the dynamics of these cycles are relatively insensitive to variations in values of the physical parameters that constitute D. With D= −2 , computed interevent periods are about 80 s, the slip distance per event is about 5 mm, maximum slip speeds are about 2 mm/s, and reduction of magma pressure during slip is about 2.4 kPa. This reduction in magma pressure is strikingly small in comparison to the ambient, roughly lithostatic magma pressure (~1.3×10^4 kPa) inferred to exist at the base of the plug, about 500 m beneath the ground surface. The small size of magma-pressure fluctuations indicates that the system deviates little from mechanical equilibrium, even during slip events. Moreover, changes in basal magma pressure during slip events can be multiplied by the inferred basal area of the plug (~30,000 m^2) to provide a proxy for the force drop available to generate seismicity.

A more refined assessment of the force drop during slip events is provided by SPASM output that shows how the shear force due to plug-boundary friction (F) evolves during slip. With $D = -2$, the computed force drop is about 7×10^7 N, and much of the force drop occurs abruptly, despite the fact that slip events have durations of ~5 s. This nearly instantaneous force drop occurs just as the slip velocity, u, decreases from a finite value to zero, and its abruptness results from the interplay of three phenomena: (1) owing to rate-weakening friction during slip, the upward-moving plug gains momentum that causes it to overshoot an equilibrium state in which forces are dynamically balanced; (2) as the upward-moving plug decelerates, a potential for downward motion exists, because basal magma pressure has relaxed to a value smaller than its static equilibrium value; and (3) incipient downward motion of the plug is arrested immediately, however, because friction along the plug margin reverses direction so as to oppose motion. Friction adjusts just enough to stop motion and balance forces, of course, because friction can only oppose motion, not drive it. The abrupt adjustment of the friction force as plug motion ceases produces a sudden force drop that can radiate high-frequency seismic energy.

The mechanics that produce the stick-slip behavior and force drops predicted by the SPASM model are robust because they derive from basic physical principles, but the weakest link in the SPASM formulation involves the nature of friction and its rate dependence. Frictional properties of granulated solids such as fault gouge are poorly understood at a fundamental level, although some degree and type of rate weakening is generally observed in a variety of both idealized and geological granular media (for example, Nasuno and others, 1997; Marone, 1998). Rate-weakening behavior has also been measured in tests of fault gouge collected from the surface of the extruding plug at Mount St. Helens (Moore and others, this volume, chap. 20). In the context of the SPASM model, the most crucial point revealed by these tests is that some degree of rate-weakening occurs as slip velocities increase from zero to a steady equilibrium value u_0. This weakening suffices to generate stick-slip behavior, regardless of subtler nuances of friction. If rate-strengthening friction develops at higher slip rates, for example, it will help arrest slip events but not prevent them. Therefore, the occurrence of stick-slip cycles appears almost inevitable.

Occurrence of stick-slip cycles large enough and abrupt enough to generate drumbeat earthquakes is also contingent on elastic properties of the magma-plug-conduit system. At least one elastic element in the system must be soft enough to strain significantly in response to driving forces that are smaller than those required to shear the fault gouge irreversibly (compare Rice and Ruina, 1983). (The shallow depths of drumbeat earthquakes implies that these driving forces are probably smaller than those causing fault slip at hypocentral depths typical of nonvolcanic earthquakes (that is, >1 km), because confining stress and frictional resistance are relatively small at depths <1 km.) At Mount St. Helens, fluid magma underlying the extruding plug provides an exceptionally soft elastic element, because its estimated 12 percent (by volume) exsolved gas content makes it orders of magnitude more compressible than solid rock. In essence, then, the magma serves as a spongy spring that compresses significantly as it delivers the force to shear the plug-bounding gouge. Strain energy stored during magma compression is released in abrupt slip events that would be smaller and more frequent if the magma were stiffer. Therefore, the earthquake cycle described by the SPASM model differs from a typical tectonic earthquake cycle in two important ways: (1) in SPASM, strain energy is stored principally in a compressed fluid, not in a solid deformed in shear; repeated, nondestructive compression of "soft" fluid enables seismogenic plug slip to occur repeatedly at shallow depths; and (2) in SPASM, after slip has ceased, the plug is reloaded by forces due to gravity and magma influx. This reloading occurs very rapidly in comparison to reloading by tectonic strain accumulation, enabling drumbeat earthquakes to occur much more frequently than tectonic earthquakes.

Gradual evolution of the magnitude and periodicity of drumbeat earthquakes observed during the 2004–5 eruption of Mount St. Helens prompts questions about the cause. Can evolution of drumbeats be a harbinger of changes in eruption rate or style? The SPASM model provides insight to this issue, but it provides no unequivocal answers. According to the model, amplitudes and periods of slip events can change in response to changes in values of any of the parameters that constitute D, even when magma ascent and solidification rates are constant. Because D encompasses the effects of gouge frictional properties and the effective stress state, as well as the natural oscillation time scale t_0, evolution of any of a number of phenomena could be responsible for changing the character of drumbeats. Nonetheless, because field data can to some degree constrain changes in quantities such as plug mass or conduit volume, it is tempting to ascribe changes in drumbeats to unobserved changes in gouge properties or the state of effective stress. Computational results from SPASM indicate that rather subtle changes in these phenomena can alter drumbeat properties significantly. Indeed, it is easy to imagine that the source of drumbeats could migrate around the periphery of the extruding plug as scattered patches of particularly strong gouge form, fail, and reform. A model more elaborate than SPASM would be required to analyze the details of such behavior.

The SPASM model does provide a clear picture of potential changes in eruption style that can occur if conditions far from equilibrium develop. One type of disequilibrium develops if the rate of magma accretion at the base of the extruding plug differs significantly from the rate of plug extrusion. If the accretion rate is less than the extrusion rate, liquid magma eventually will reach the ground surface. Magma pressure will simultaneously decline, and this decline could enhance magma vesiculation and explosive potential. On the other hand, if the plug accretion rate exceeds the extrusion rate, the solidification front will propagate downward and magma pressure will increase, assuming that deep magma influx remains constant.

Increasing pressure could eventually trigger an exceptionally large slip event or fracture surrounding rock, causing a transition in eruption style—or it could suffice to stop magma influx, thereby halting the eruption.

Effects of magma pressure exceeding the static limiting equilibrium pressure can be treated as disequilibrium initial conditions in the SPASM model. If excess pressure exists but is insufficient to fracture rock, a rapid pulse of plug motion occurs until static equilibrium is restored. If magma pressure exceeds the equilibrium pressure by even a few percent, SPASM predicts that this pulse can involve velocities of meters per second and displacements of many meters. Such a pulse could even eject the plug from the volcanic vent and instigate the type of transition in eruption style described above.

The fact that no rapid pulses of extrusion or transitions in eruption style occurred during the 2004–5 eruption of Mount St. Helens implies that the magma-plug system never deviated much from equilibrium, even during the eruption onset. This behavior is, of course, very different from that during the cataclysmic eruption of Mount St. Helens on May 18, 1980. In that case explosive activity was caused by rapid depressurization of a shallow magma body triggered by a massive landslide. Without the landslide trigger, the 1980 eruptions of Mount St. Helens might have been relatively quiescent, much like the eruption of 2004–5.

Conclusion

The central conclusion of this study is that stick-slip oscillations are almost inevitable during an eruption in which steady ascent of compressible magma drives upward extrusion of a solidified plug with margins that exhibit rate-weakening friction. Whether such oscillations are large and abrupt enough to generate repetitive earthquakes like those observed at Mount St. Helens depends on a host of factors, nearly all of which are encompassed within two quantities derived in this paper: the natural oscillation time scale $t_0 = [m_0(\alpha_1 + \alpha_2)V_0]^{1/2} / A$ and the frictional damping index, which can be approximated as $D \approx (1/2)\left(c\,\lambda\,\mu_0\,g\,t_0 / u_0\right)$. Large values of t_0 favor the occurrence of relatively large, infrequent slip events, because they imply that large elastic strains can be accommodated during magma compression. Large negative values of D have similar effects because they imply that effects of rate-weakening plug friction are significant, and rate weakening is responsible for "dynamic overshoot" during slip events. As a consequence, negative D values far from 0 cause the period between successive slip effects to exceed the period expected on the basis of t_0 alone.

Computations using $D = -2$ predict the occurrence of stick-slip cycles with interevent periods of ~80 s, slip displacements of ~5 mm, and force drops of ~7×10^7 N, and these properties appear consistent with those of events inferred to produce drumbeat earthquakes during the 2004–5 eruption of Mount St. Helens. Although individual modeled slip events last about 5 s, most of the accompanying force drop occurs in a fraction of a second, consistent with requirements for radiation of high-frequency seismic energy.

Persistence of nearly periodic drumbeat earthquakes also requires that slip events are driven by nearly steady forcing. At Mount St. Helens this forcing was provided by nearly steady ascent of magma. Magma solidification at the base of the extruding plug apparently occurred at a rate nearly equal to the rate of magma ascent, enabling the system to remain close to equilibrium. Indeed, model results show that a near-balance between ascent rate and solidification rate is essential for maintaining persistent drumbeats.

The presence of a near-surface body of compressible magma that serves as a driving element may be necessary to generate repetitive, seismogenic stick-slip events at the shallow focal depths (<1 km) observed during the 2004–5 eruption of Mount St. Helens. The strength of gouge at such shallow depths is relatively small (owing to relatively small normal stresses), and the gouge can therefore shear irreversibly before much elastic strain accumulates in a stiff adjacent body such as solid rock. Therefore, in the absence of a soft, near-surface magma body, stick-slip oscillations could still occur, but they would be reduced in size and period, perhaps to a degree that would make them aseismic. Moreover, near-surface fluid magma can undergo repeated elastic compression and decompression without accumulation of irreversible damage that would likely accompany similarly repetitive strain in solid rock.

Lack of large movement pulses during the 2004–5 eruption of Mount St. Helens reinforces the view that the magma-plug system remained close to equilibrium. Indeed, model results indicate that magma pressure exceeding the static equilibrium pressure by even a few percent was probably never present. An implication of this finding is that the dynamic equilibrium state exhibited during the eruption differs little from the static equilibrium state before the eruption onset. Therefore, the eruption trigger was likely very subtle, perhaps involving nothing more than weakening of the conduit cap rock by percolating water derived from late summer rains and glacier melt.

Acknowledgments

Virtually every member of the staffs of the Cascades Volcano Observatory and Pacific Northwest Seismic Network helped make this work possible through their contributions to monitoring the 2004–5 eruption of Mount St. Helens. I am indebted to all of them for their extraordinary efforts, and particularly to Seth Moran for fielding my many questions about volcano seismology. I am also indebted to Nico Gray of the Department of Mathematics, University of Manchester, U.K., who showed me how to obtain the analytical results summa-

rized in equations 33–37 and appendix 1, and to Peter Moore and Neal Iverson, Department of Geological and Atmospheric Sciences, Iowa State University, who performed laboratory tests of the frictional properties of the Mount St. Helens gouge. Roger Denlinger and Joseph Walder provided insightful reviews that helped improve the manuscript.

References Cited

Abramowitz, M.K., and Stegun, I.A., eds., 1964, Handbook of mathematical functions with formulas, graphs, and mathematical tables: Washington, D.C., U.S. Government Printing Office, U.S. National Bureau of Standards Applied Mathematic Series 55, 1046 p.

Beeler, N.M., Tullis, T.E., and Weeks, J.D., 1994, The roles of time and displacement in the evolution effect in rock friction: Geophysical Research Letters, v. 21, no. 18, p. 1987–1990.

Blundy, J., and Cashman, K., 2001, Ascent-driven crystallisation of dacite magmas at Mount St. Helens, 1980–1986: Contributions to Mineralogy and Petrology, v.140, no. 6, p. 631–650, doi:10.1007/s004100000219.

Denlinger, R.P., and Hoblitt, R.P., 1999, Cyclic eruptive behavior of silicic volcanoes: Geology, v. 27, p. 459–462.

Dieterich. J.H., 1979, Modeling of rock friction 1; experimental results and constitutive equations: Journal of Geophysical Research, v. 84, no. B5, p. 2161–2168.

Dzurisin, D., Vallance, J.W., Gerlach, T.M., Moran, S.C., and Malone, S.D., 2005, Mount St. Helens reawakens: Eos (American Geophysical Union Transactions), v. 86, p. 25, 29.

Dzurisin, D., Lisowski, M., Poland, M.P., Sherrod, D.R., and LaHusen, R.G., 2008, Constraints and conundrums resulting from ground-deformation measurements made during the 2004–2005 dome-building eruption of Mount St. Helens, Washington, chap. 14 *of* Sherrod, D.R., Scott, W.E., and Stauffer, P.H., eds., A volcano rekindled; the renewed eruption of Mount St. Helens, 2004–2006: U.S. Geological Survey Professional Paper 1750 (this volume).

Gerlach, T.M., McGee, K.A., and Doukas, M.P., 2008, Emission rates of CO_2, SO_2, and H_2S, scrubbing, and preeruption excess volatiles at Mount St. Helens, 2004–2005, chap. 26 *of* Sherrod, D.R., Scott, W.E., and Stauffer, P.H., eds., A volcano rekindled; the renewed eruption of Mount St. Helens, 2004–2006: U.S. Geological Survey Professional Paper 1750 (this volume).

Goto, A., 1999, A new model for volcanic earthquake at Unzen volcano; melt rupture model: Geophysical Research Letters, v. 26, no. 16, 2541–2544.

Hatheway, A.W., and Kiersch, G.A., 1989, Engineering properties of rock, *in* Carmichael, R.S., ed., Practical handbook of the physical properties of rocks and minerals: Boca Raton, Florida, CRC Press, p. 673–715.

Kreyszig, E., 1979, Advanced engineering mathematics (4th ed.): New York, John Wiley, 939 p.

Lahr, J.C., Chouet, B.A., Stephens, C.D., Power, J.A., and Page, R.A., 1994, Earthquake classification, location, and error analysis in a volcanic environment; implications for the magmatic system of the 1989–1990 eruptions at Redoubt Volcano, Alaska: Journal of Volcanology and Geothermal Research, v. 62, nos. 1–4, p. 137–151, doi:10.1016/0377-0273(94)90031-0.

LaHusen, R.G., Swinford, K.J., Logan, M., and Lisowski, M., 2008, Instrumentation in remote and dangerous settings; examples using data from GPS "spider" deployments during the 2004–2005 eruption of Mount St. Helens, Washington, chap. 16 *of* Sherrod, D.R., Scott, W.E., and Stauffer, P.H., eds., A volcano rekindled; the renewed eruption of Mount St. Helens, 2004–2006: U.S. Geological Survey Professional Paper 1750 (this volume).

Lisowski, M., Dzurisin, D., Denlinger, R.P., and Iwatsubo, E.Y., 2008, Analysis of GPS-measured deformation associated with the 2004–2006 dome-building eruption of Mount St. Helens, Washington, chap. 15 *of* Sherrod, D.R., Scott, W.E., and Stauffer, P.H., eds., A volcano rekindled; the renewed eruption of Mount St. Helens, 2004–2006: U.S. Geological Survey Professional Paper 1750 (this volume).

Losert, W., Géminard, J.C., Nauson, S., and Gollub, J.P., 2000, Mechanisms for slow strengthening of granular materials: Physical Review E, v. 61, p. 4060–4068.

Major, J.J., Kingsbury, C.G., Poland, M.P., and LaHusen, R.G., 2008, Extrusion rate of the Mount St. Helens lava dome estimated from terrestrial imagery, November 2004–December 2005, chap. 12 *of* Sherrod, D.R., Scott, W.E., and Stauffer, P.H., eds., A volcano rekindled; the renewed eruption of Mount St. Helens, 2004–2006: U.S. Geological Survey Professional Paper 1750 (this volume).

Marone, C., 1998, Laboratory-derived friction laws and their application to seismic faulting: Annual Review of Earth and Planetary Sciences, v. 26, p. 643–696.

Marone, C., and Richardson, E., 2006, Do earthquakes rupture piece by piece or all together?: Science, v. 313, p.1748-1749.

Mastin, L.G., 1994, Explosive tephra emissions at Mount St. Helens, 1989–1991; the violent escape of magmatic gas following storms?: Geological Society of America Bulletin, v. 106, no. 2, p. 175–185.

Mastin, L.G., and Ghiorso, M.S., 2000, A numerical program for steady-state flow of magma-gas mixtures through vertical eruptive conduits: U.S. Geological Survey Open-File Report 00–209, 56 p.

Mastin, L.G., Roeloffs, E., Beeler, N.M., and Quick, J.E., 2008, Constraints on the size, overpressure, and volatile content of the Mount St. Helens magma system from geo-

detic and dome-growth measurements during the 2004–2006+ eruption, chap. 22 *of* Sherrod, D.R., Scott, W.E., and Stauffer, P.H., eds., A volcano rekindled; the renewed eruption of Mount St. Helens, 2004–2006: U.S. Geological Survey Professional Paper 1750 (this volume).

McGarr, A., 1999, On relating apparent stress to the stress causing earthquake slip: Journal of Geophysical Research, v. 104, no. B2, p. 3003–3011.

Melnik, O., and Sparks, R.S.J., 2002, Dynamics of magma ascent and lava extrusion at Soufrière Hills Volcano, Montserrat, *in* Druitt, T.H., and Kokelaar, B.P., eds., The eruption of Soufrière Hills Volcano, Montserrat, from 1995 to 1999: Geological Society of London Memoir 21, p. 153–171.

Moore, P.L., Iverson, N.R., and Iverson, R.M., 2008, Frictional properties of the Mount St. Helens gouge, chap. 20 *of* Sherrod, D.R., Scott, W.E., and Stauffer, P.H., eds., A volcano rekindled; the renewed eruption of Mount St. Helens, 2004–2006: U.S. Geological Survey Professional Paper 1750 (this volume).

Moran, S.C., 1994, Seismicity at Mount St. Helens, 1987–1992; evidence for repressurization of an active magmatic system: Journal of Geophysical Research, v. 99, no. B3, p. 4341–4354, doi:10.1029/93JB02993.

Moran, S.C., Malone, S.D., Qamar, A.I., Thelen, W.A., Wright, A.K., and Caplan-Auerbach, J., 2008, Seismicity associated with renewed dome building at Mount St. Helens, 2004–2005, chap. 2 *of* Sherrod, D.R., Scott, W.E., and Stauffer, P.H., eds., A volcano rekindled; the renewed eruption of Mount St. Helens, 2004–2006: U.S. Geological Survey Professional Paper 1750 (this volume).

Mullineaux, D.R., and Crandell, D.R., 1981, The eruptive history of Mount St. Helens, *in* Lipman, P.W., and Mullineaux, D.R., eds., The 1980 eruptions of Mount St. Helens, Washington: U.S. Geological Survey Professional Paper 1250, p. 3–15.

Nasuno, S., Kudrolli, A., and Gollub, J.P., 1997, Friction in granular layers; hysteresis and precursors: Physical Review Letters, v. 79, p. 949–952.

Neuberg, J.W., 2000, Characteristics and causes of shallow seismicity in andesite volcanoes: Philosophical Transactions Royal Society of London A, v. 358, p. 1533–1546.

Neuberg, J.W., Tuffen, H., Collier, L., Green, D., Powell, T., and Dingwell, D., 2006, The trigger mechanism of low-frequency earthquakes at Montserrat: Journal of Volcanology and Geothermal Research, v. 153, nos. 1–2, p. 37–50, doi:10.1016/j.jvolgeores.2005.08.008.

Newman, S., and Lowenstern, J.B., 2002, VolatileCalc—a silicate melt-H2O-CO2 solution model written in Visual Basic for excel®: Computers and Geosciences, v. 28, no. 5, p. 597–604, doi:10.1016/S0098-3004(01)00081-4.

Ozerov, A., Ispolatov, I., and Lees, J., 2003, Modeling Strombolian eruptions of Karymsky volcano, Kamchatka, Russia: Journal of Volcanology and Geothermal Research, v. 122, p. 265–280.

Pallister, J.S., Reagan, M., and Cashman, K., 2005, A new eruptive cycle at Mount St. Helens?: Eos (American Geophysical Union Transactions), v. 86, p. 499.

Pallister, J.S., Thornber, C.R., Cashman, K.V., Clynne, M.A., Lowers, H.A., Mandeville, C.W., Brownfield, I.K., and Meeker, G.P., 2008, Petrology of the 2004–2006 Mount St. Helens lava dome—implications for magmatic plumbing and eruption triggering, chap. 30 *of* Sherrod, D.R., Scott, W.E., and Stauffer, P.H., eds., A volcano rekindled; the renewed eruption of Mount St. Helens, 2004–2006: U.S. Geological Survey Professional Paper 1750 (this volume).

Press, W.H., Flannery, B.P., Teukolsky, S.A., and Vettering, W.T., 1986, Numerical recipes the art of scientific computing: Cambridge, Cambridge University Press, 818 p.

Rice, J.R., and Ruina, A., 1983, Stability of steady frictional slipping: Journal of Applied Mechanics, v. 50, p. 343–349.

Ruina, A., 1983, Slip instability and state variable friction laws: Journal of Geophysical Research, v. 88, no. B12, p. 10359–10370.

Schilling, S.P., Carrara, P.E., Thompson, R.A., and Iwatsubo, E.Y., 2004, Posteruption glacier development within the crater of Mount St. Helens, Washington, USA: Quaternary Research, v. 61, no. 3, p. 325–329.

Schilling, S.P., Thompson, R.A., Messerich, J.A., and Iwatsubo, E.Y., 2008, Use of digital aerophotogrammetry to determine rates of lava dome growth, Mount St. Helens, Washington, 2004–2005, chap. 8 *of* Sherrod, D.R., Scott, W.E., and Stauffer, P.H., eds., A volcano rekindled; the renewed eruption of Mount St. Helens, 2004–2006: U.S. Geological Survey Professional Paper 1750 (this volume).

Scholz, C.H., 2002, The mechanics of earthquakes and faulting (2d ed.): Cambridge, Cambridge University Press, 471 p.

Swanson, D.A., and Holcomb, R.T., 1990, Regularities in growth of the Mount St. Helens dacite dome, 1980–1986, *in* Fink, J.H., ed., Lava flows and domes, emplacement mechanisms and hazard implications: Berlin, Springer-Verlag, International Association of Volcanology and Chemistry of the Earth's Interior, Proceedings in Volcanology 2, p. 3–24.

Tuffen, H., and Dingwell, D., 2005, Fault textures in volcanic conduits; evidence for seismic trigger mechanisms during silicic eruptions: Bulletin of Volcanology, v. 67, p. 370–387.

Voight, B., and 24 others, 1999, Magma flow instability and cyclic activity at Soufriere Hills Volcano, Montserrat, British West Indies: Science, v. 238, p. 1138–1142.

Walder, J.S., LaHusen, R.G., Vallance, J.W., and Schilling, S.P., 2005, Crater glaciers on active volcanoes; hydrological anomalies: Eos (American Geophysical Union Transactions), v. 86, p. 521, 528.

Appendix 1. Solution of Equation 27 by Transformation to Bessell's Equation

Conversion of the homogenous part of equation 27 into Bessel's equation is accomplished by using a simultaneous change of independent and dependent variables, given by

$$t^* = \frac{1}{K}\left[\left(\frac{K\,z}{2}\right)^2 - 1\right] \qquad u^* = w\left(\frac{z}{2}\right)^{\frac{K-2D}{K}}. \tag{A1}$$

Substitution of equation group A1 into equation 27 converts it into Bessel's differential equation

$$z^2\frac{d^2w}{dz^2} + z\frac{dw}{dz} + (z^2 - \nu^2)\,w = 0, \tag{A2}$$

where

$$\nu = \frac{K-2D}{K}. \tag{A3}$$

The general solution of Bessel's equation is

$$w = c_1 J_\nu(z) + c_2 Y_\nu(z), \tag{A4}$$

where c_1 and c_2 are arbitrary constants and J_ν and Y_ν are Bessel functions of the first and second kind, of order ν (Abramowitz and Stegun, 1964). Equation 33 is obtained by transforming equation A4 back to the original variables t^* and u^* and adding a particular solution of the inhomogeneous version of equation 27, $u^* = -KG$.